Three-dimensional geometry of axial magma chamber roof and faults at Lucky Strike volcano on the Mid-Atlantic Ridge

Violaine Combier, Tim Seher, Satish Singh, Wayne Crawford, Mathilde Cannat, Javier Escartin, Doga Dusunur

AGU PUBLICATIONS

JGR

Journal of Geophysical Research: Solid Earth

RESEARCH ARTICLE
10.1002/2015JB012365

Key Points:
- Lucky Strike volcano magma chamber and faults are imaged by 3-D seismic reflection
- Insights into magmatic and tectonic processes at a slow spreading mid-ocean ridge are provided
- 3-D seismic reflection processing provides a high-resolution bathymetric map of the volcano

Supporting Information:
- Texts S1 and S2 and Figure S1

Correspondence to:
V. Combier,
vcombier@gmail.com

Citation:
Combier, V., T. Seher, S. C. Singh, W. C. Crawford, M. Cannat, J. Escartín, and D. Dusunur (2015), Three-dimensional geometry of axial magma chamber roof and faults at Lucky Strike volcano on the Mid-Atlantic Ridge, *J. Geophys. Res. Solid Earth*, *120*, 5379–5400, doi:10.1002/2015JB012365.

Received 16 JUL 2015
Accepted 16 JUL 2015
Accepted article online 21 JUL 2015
Published online 19 AUG 2015

Three-dimensional geometry of axial magma chamber roof and faults at Lucky Strike volcano on the Mid-Atlantic Ridge

Violaine Combier[1], Tim Seher[1], Satish C. Singh[2], Wayne C. Crawford[2], Mathilde Cannat[2], Javier Escartín[2], and Doga Dusunur[3]

[1]Formerly at Géosciences Marines, Institut de Physique du Globe, Paris, France, [2]Géosciences Marines, Institut de Physique du Globe, Paris, France, [3]Department of Geophysical Engineering, Istanbul Technical University, Istanbul, Turkey

Abstract We present results from three-dimensional (3-D) processing of seismic reflection data, acquired in June 2005 over the Lucky Strike volcano on the Mid-Atlantic Ridge as a part of the Seismic Study for Monitoring of the Mid-Atlantic Ridge survey. We use a 3-D tomographic velocity model derived from a coincident ocean bottom seismometer experiment to depth convert the poststack time-migrated seismic volume and provide 3-D geometry of the axial magma chamber roof, fault reflectors, and layer 2A gradient marker. We also generate a high-resolution bathymetric map using the seismic reflection data. The magma chamber roof is imaged at 3.4 ± 0.4 km depth beneath the volcano, and major faults are imaged with dips ranging between 33° and 50°. The magma chamber roof geometry is consistent with a focused melt supply at the segment center and steep across-axis thermal gradients as indicated by the proximity between the magma chamber and nearby faults. Fault scarps on the seafloor and fault dip at depth indicate that tectonic extension accounts for at least 10% of the total plate separation. Shallow dipping reflectors imaged in the upper crust beneath the volcano flanks are interpreted as buried lava flow surfaces.

1. Introduction

The process of oceanic crustal accretion is less-well understood at slow spreading than at fast spreading oceanic spreading centers. A crustal melt lens is ubiquitously observed by seismic reflection studies beneath fast spreading centers but, until recently, only limited geophysical evidence was found for the presence of a crustal melt lens at slow spreading centers. Seismic refraction experiments (e.g., MARK [*Canales et al.*, 2000] or OH-1 [*Hooft et al.*, 2000]) found evidence for interstitial crustal melt, but no melt lens reflector was imaged despite several reconnaissance multichannel seismic reflection profiles across portions of the Mid-Atlantic Ridge (MAR) rift valley [e.g., *Detrick et al.*, 1990; *Sinton and Detrick*, 1992]. Moreover, microearthquake [e.g., *Toomey et al.*, 1985] and teleseismic [e.g., *Huang and Solomon*, 1988] studies have shown that earthquakes can occur down to depths of 8 km or more beneath the median valley of the MAR, suggesting the cooling of the entire crustal section to temperatures within the brittle regime. These studies led to the belief that slow spreading ridge crustal magma chambers were of small extent and short lived [*Sinton and Detrick*, 1992; *Cannat*, 1993].

More recent seismic reflection studies have revealed evidence for crustal melt lenses or bodies beneath slow spreading centers. The Reykjanes Axial Melt Experiment: Structural Synthesis from Electromagnetics and Seismics at 57°45′N [e.g., *Sinha et al.*, 1998; *Peirce et al.*, 2007] revealed a seismic reflector 2.5–3 km beneath the seafloor on the Reykjanes Ridge underlain by a larger low-velocity zone interpreted as a magma chamber that could contain up to 20% melt. Subsequently, the Seismic Study for Monitoring of the Mid-Atlantic Ridge (SISMOMAR) seismic reflection experiment imaged a bright crustal reflector beneath the central volcano of the Lucky Strike segment of the MAR, interpreted as the roof a magma chamber [*Singh et al.*, 2006]. The bright reflector overlies a low-velocity zone of decreased velocities that can be explained by elevated temperatures (800–1000°C) and possibly a small amount of melt [*Seher et al.*, 2010a].

Singh et al. [2006] used 2-D processing and showed the result as a function of two-way time beneath the volcano. Here we present results obtained using a complete 3-D processing of the SISMOMAR reflection data in the time domain followed by depth conversion, which allows us to constrain the geometry of the

axial magma chamber roof, faults, layer 2A, and other seismic events within the upper crust and provides a detailed map of the seafloor topography. We use these results to shed light on the magmatic and tectonic processes that are involved in the formation and evolution of the oceanic crust at slow spreading ridges with robust melt supply to the axis.

2. Geological Context

The Lucky Strike volcano, located at ~37°17′N along the Mid-Atlantic Ridge (MAR), is situated at the center of the 70 km long Lucky Strike segment (Figure 1a). The Lucky Strike segment, which has a full spreading rate of ~2.1 cm/yr [*Demets et al.*, 1994], is located approximately 400 km southwest of the Azores hot spot's probable location [*Zhang and Tanimoto*, 1992; *Schilling*, 1991; *Ito and Lin*, 1995; *Moreira et al.*, 1999]. The segment's basalt geochemistry [*Dosso et al.*, 1999; *Gale et al.*, 2011] and topography [*Detrick et al.*, 1995] indicate that it is influenced by the hot spot. An along-axis southward propagation of a magmatic pulse from the Azores hot spot is indicated by V-shaped ridges and by two anomalously shallow regions, the eastern and western Jussieu plateaus, located on either side of the MAR at the latitudes of the Famous (36°50′N) and Lucky Strike segments [*Cannat et al.*, 1999; *Escartin et al.*, 2001; *Gente et al.*, 2003]. More generally, the Mid-Atlantic Ridge deepens gradually southward from the Azores region near 40°N (axial depth: 1800 m on average [*Detrick et al.*, 1995]) to about 26°N (axial depth: 3850 m on average [*Thibaud et al.*, 1998]). This long-wavelength bathymetric gradient coexists with similarly long gradients of gravity anomalies and basalt geochemistry, suggesting that regional crustal thickness, the buoyancy of the upper mantle beneath the ridge, and its content in incompatible elements (characteristic of the lower mantle composition) all decrease slowly away from the Azores region [*Vogt*, 1976; *Schilling*, 1985]. These gradients indicate that the plume of anomalously hot and/or enriched mantle (hot spot) thought to feed volcanism in the Azores islands also influences the nearby Mid-Atlantic Ridge over more than a thousand kilometers along axis.

In spite of its proximity to the Azores hot spot, the Lucky Strike segment exhibits a morphological and tectonic architecture with many of the characteristics of a slow spreading ridge. The Lucky Strike segment is characterized by a well-developed, ~13–20 km wide axial rift valley, whose depth increases from ~1550 m at the segment center to ~3700 m at the nodal basins near the segment ends (Figure 1a). Two major normal faults (hereafter called the eastern and western bounding faults, EBF and WBF) bound the rift valley with vertical throws of 500–900 m. Beyond the rift walls, the seafloor morphology is dominated by fault-controlled abyssal hills [*Detrick et al.*, 1995]. The center of the segment is dominated by the 8 km wide, 15 km long, and 500 m high Lucky Strike volcano, one of the largest central volcanoes along the MAR axis. The SISMOMAR experiment [*Singh et al.*, 2006; *Dusunur et al.*, 2009; *Crawford et al.*, 2010; *Seher et al.*, 2010a, 2010b, 2010c; *Arnulf et al.*, 2012, 2013, 2014] provided seismic data used to characterize the magma chamber beneath the volcano: the roof of the axial magma chamber (AMC) imaged by multichannel seismic reflection [*Singh et al.*, 2006] is underlain by a low-velocity zone imaged by travel time tomography of ocean bottom seismic data [*Seher et al.*, 2010a]. The crust is ~7.5 km thick beneath the volcano and has thinned to less than 5.5 km at 20 km from the segment center [*Crawford et al.*, 2010; *Seher et al.*, 2010a]. *Arnulf et al.* [2014] studied the first kilometer of the upper crust with travel time tomography and full waveform inversion of downward continued streamer data. Their studies suggest that seismic layer 2A within the volcano is anomalously thick and displays low seismic velocities, consistent with the emplacement of a $>$700–900 m thick sequence of extrusives [*Arnulf et al.*, 2014].

The volcano summit shows three local highs enclosing a depression where lava recently ponded [*Fouquet et al.*, 1995; *Ondréas et al.*, 2009; *Humphris et al.*, 2002]. The depression is part of a recent axial graben up to ~1 km in width that dissects the volcano (axial graben Ra on Figure 1b) [*Escartín et al.*, 2014]. The depression is surrounded by numerous hydrothermal vents that constitute one of largest hydrothermal sites on the MAR, extending over ~1 km^2, with numerous active and inactive vents and zones of diffuse flow [e.g., *Fouquet et al.*, 1995; *Langmuir et al.*, 1997; *von Damm et al.*, 1998; *Humphris et al.*, 2002; *Barreyre et al.*, 2012] (Figure 1b).

A microseismic experiment conducted in the area revealed microseismic events in the immediate vicinity of the AMC [*Dusunur et al.*, 2009] and sustained activity above the AMC and along the most recent graben attributed to cooling associated with along-axis hydrothermal cells feeding the volcano summit vent field [*Crawford et al.*, 2013]. Hydroacoustic monitoring in the area also suggests that a dike intrusion

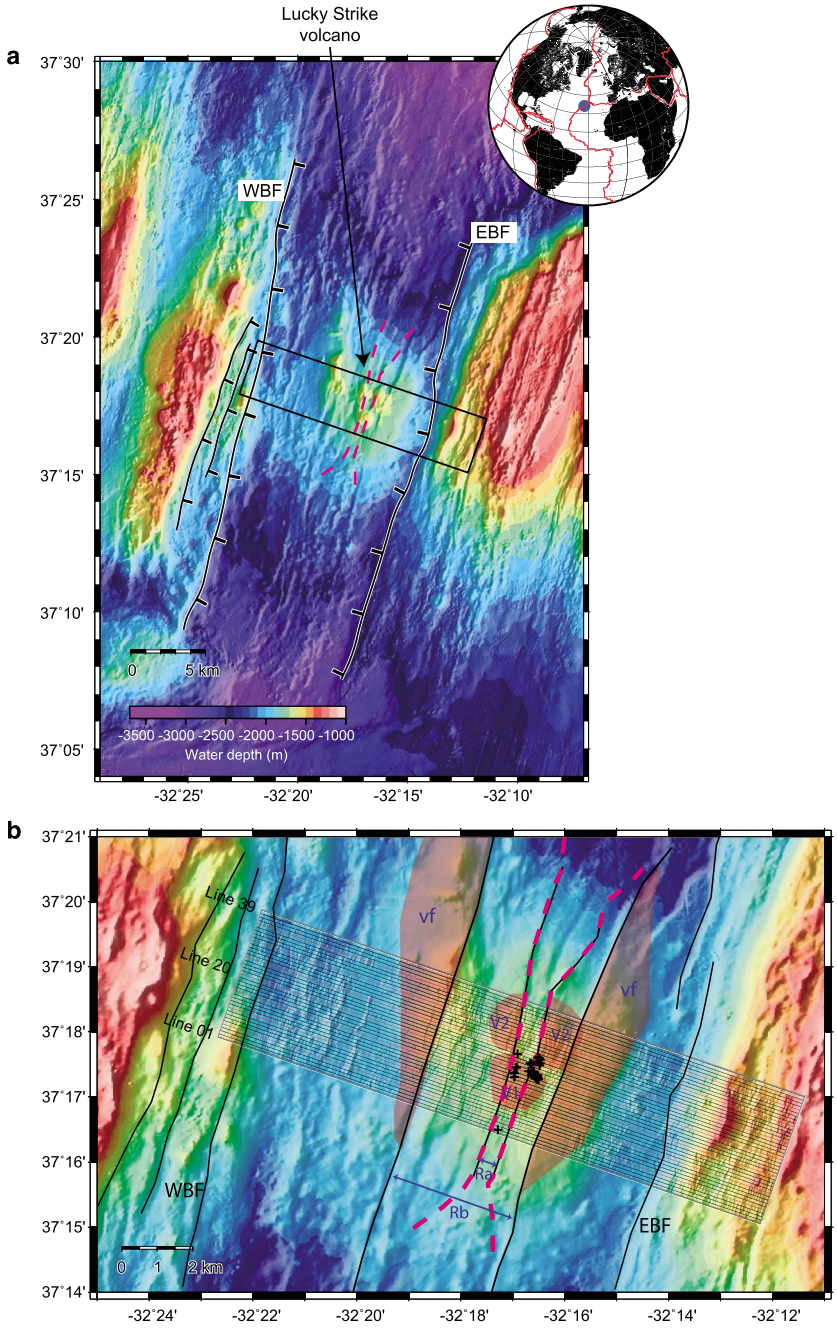

Figure 1. (a) Location of the 3-D seismic reflection survey on the Lucky Strike segment bathymetry. WBF: western bounding fault, EBF: eastern bounding fault. The 3-D seismic reflection area is outlined by the black rectangle. Neovolcanic zone [*Escartín et al.*, 2014] is outlined by pink dashed lines. (b) The 3-D seismic reflection survey area. Small crosses indicate the location of known Lucky Strike hydrothermal vents. Structural interpretation of the volcano from *Escartín et al.* [2014] is reported. Unfaulted initial volcano flanks (vf) and two more recent volcanic cones (v2 and v1) are colored in red. The initial volcano with flanks (vf) was emplaced within the axial valley bounded by the EBF and WBF. Then, two successive axial grabens dissected the volcano (Rb and Ra). The most recent axial graben, Ra, has dissected the two summit volcanic cones (v1 and v2). The neovolcanic zone (coutours outlined by pink dashed lines) is focused within graben Ra.

or volcanic eruption may have taken place within the segment in 2001 [*Dziak et al.*, 2004], although no seafloor observations were available to document a possible seafloor eruption and subsequent observations in the area have not identified any structures that may be associated with such an event (e.g., fresh-looking lava flows).

On the volcano summit, the neovolcanic zone—determined from seafloor texture on side scan data [*Scheirer et al.*, 2000; *Escartín et al.*, 2014] and near-bottom observations [*Ondréas et al.*, 1997; *Humphris et al.*, 2002]—is focused within the most recent axial graben. North and south of the summit, the neovolcanic zone is less focused and widens [*Escartín et al.*, 2014]. Recent pillow lavas were also observed on a volcanic edifice northwest of the volcano summit, known as the western volcanic ridge [*Ondréas et al.*, 1997]. The present-day spreading axis determined from ship-board magnetic data [*Miranda et al.*, 2005] is displaced slightly east of the neovolcanic zone. Magnetic anomaly modeling using the present-day magnetic axis as a fixed spreading axis suggests that spreading has been asymmetric with faster spreading to the west over the past 0.7 Ma [*Miranda et al.*, 2005], which is the period during which the present-day axial valley and Lucky Strike volcano were built.

The history of volcano emplacement and rifting inferred for the area also suggests a complex magmatic and tectonic history [*Escartín et al.*, 2014]. The Lucky Strike central volcano is emplaced at the center and within the main rift valley, but its structure shows several episodes of successive rifting and volcanic emplacement at its summit (Figure 1b), which likely correspond to recent periods of decreased and increased eruption rates [*Escartín et al.*, 2014], demonstrating important interactions between faulting and volcanism.

3. Survey Design and Data Acquisition

The SISMOMAR experiment is a seismic reflection and refraction study of the crustal structure beneath the Lucky Strike segment of the MAR [*Crawford et al.*, 2010], conducted on board the Research Vessel Atalante in June–July 2005. The experiment was composed of a 3-D multichannel seismic reflection box (18.75 km long, 3.8 km wide; Figure 1b), a 3-D seismic wide-angle box (50 × 50 km) [*Seher et al.*, 2010a], and 2-D seismic tomography and reflection lines along and across the ridge axis [*Crawford et al.*, 2010]. In addition, microearthquake data were collected during the time windows when no active seismic source was used, totaling 6 days [*Dusunur et al.*, 2009]. The seismic reflection experiment is the first 3-D seismic reflection survey of a magma chamber on a slow spreading ridge.

Three-dimensional seismic reflection data were acquired using a 4.5 km long digital streamer towed at ~15 m depth. The streamer was composed of 360 channels with 12.5 m receiver group intervals. The minimum offset (i.e., the offset between the source and the first trace on the streamer) was 191 m, and the maximum offset was 4681 m. The energy source was a 42.5 L 18 air gun array towed at a depth of ~12 m and tuned to provide a source with a strong first arrival and a wide frequency range of 8–50 Hz.

The 3-D seismic reflection survey zone was designed to image the crust beneath the central part of the volcano. Thirty-nine 18.75 km long seismic reflection lines were shot, spaced 100 m apart (Figure 1b). To obtain a high-resolution image across the ridge axis, lines were shot perpendicular to the ridge axis (109° azimuth), with a shot interval of 37.5 m. These survey parameters resulted in a common midpoint (CMP) spacing of 6.25 m along the shooting direction and nominal fold of 60 (each CMP was in theory covered by 60 traces, corresponding to 60 different source-receiver offsets). The full-fold area is 16.25 km × 3.8 km after elastic binning (the binning process is explained in the supporting information). The vessel speed was 4.5 knots, the record length was 11 s, and the sample interval was 2 ms. It took just under 7 days to shoot the 39 lines, with 49% of the time spent on actual lines, and 51% of the time spent on turns. The data were resampled at 4 ms interval out to 6 s for the present study.

The dimensions of a 3-D survey area should be defined in such a way that dipping reflectors are correctly imaged. The energy reflecting with zero-offset from a point P at depth Z on a reflector dipping with angle α is recorded at the surface with a horizontal distance of $X = Z \tan \alpha$ away from P in the downdip direction in a constant velocity medium ($X \leq Z \tan \alpha$ in a medium where velocity increases with depth). Therefore, for the steepest dip (~35°) at the seafloor (~2 km depth) in the across-axis direction, we require $X = 1.4$ km, whereas for the steepest dip at the seafloor in the along-axis direction (~15°), we require $X = 0.6$ km. Our survey area dimensions (16.25 km × 3.8 km), thus, allow us to correctly image the volcano and axial valley seafloor morphology. At 5 km depth, dips of 55°, typical of fault dips, are recorded with zero-offset at a distance $X \leq 7$ km. Our survey dimensions, thus, allow us to image all axis-parallel ridgeward dipping faults in the survey area. The maximum dip in the along-axis direction that can be imaged at 5 km depth at the center of the survey zone is 20°.

In order to migrate dipping reflectors or to correctly collapse dipping branches of hyperbolae, CMP spacing should satisfy the following criteria: $f_{max} = v/(4\ \Delta x \sin\theta)$, where f_{max} is the maximum frequency that is not aliased for a structural dip θ, a CMP trace spacing Δx, in a medium of velocity v.

In our case, the 6.25 m inline CMP spacing theoretically allows us to image all possible dips, as the maximum unaliased frequency for 90° dips is 60 Hz at water velocity. By contrast, the 100 m crossline CMP spacing is too coarse to allow proper imaging of dipping events ($f_{max} = 11$ Hz for 20° dips at 1500 m/s) but was chosen for economic reasons since aliasing problems can be successfully overcome by trace interpolation without compromising the accuracy of the 3-D imaging, as will be explained later.

4. Processing

Accurate positioning of source and receivers for each shot is essential for 3-D processing. The position of the ship was measured using a differential GPS, and the shape of the streamer was reconstructed using 16 compass birds along the streamer and a GPS on the tail-buoy. The method used for reconstructing the streamer shape is described in the supporting information.

We performed conventional 3-D processing, including elastic binning into 6.25 m inline × 100 m crossline bins with an elastic bin size of 18.75 m inline × 200 m crossline (the elastic binning method is described in the supporting information), resampling to 4 ms, band-pass filter 5–50 Hz, predictive deconvolution with a 12 ms gap to attenuate ringing from the air gun source, normal moveout (NMO), mute of the seafloor multiple and far offsets, 3-D dip moveout, spherical divergence correction, stack, poststack trace interpolation in the crossline direction, 3-D time migration, gain application (proportional to $v^2(t).t$, where t is the two-way travel time and $v(t)$ is the root-mean-square velocity derived from travel time tomography, as an approximation to take into account attenuation [*Newman*, 1973]), and depth conversion. No trace editing was applied, because stacking gave similar results with and without noisy trace edition. A complete description of the seismic processing is given in *Combier* [2007].

4.1. Velocity and Offset Analysis

To perform velocity analysis, we used the constant velocity stack (CVS) method instead of a velocity spectrum method (such as the semblance method). The CVS method consists of performing stacks using a range of constant NMO velocity values, which allows the interpreter to directly choose the velocities yielding the stack with the best possible event continuity. It is especially useful in areas with rough seafloor topography where the data are contaminated by energy scattered at the seafloor that can show a strong coherency on CMP gathers, but that does not show lateral continuity on the stacked sections.

Analysis performed on CMP gathers (Figure 2) and on "partial" stacks, including selected offset ranges (<1500 m, 1500–3500 m, and >3500 m; Figure 3), allowed us to characterize different events in the data. A subhorizontal event is present beneath the volcano, at ~3.75 s (i.e., ~1.5 s after the seafloor arrival) stacking at velocities ranging between 2500 and 3200 m/s. This event is a true reflection (energy starts arriving at short offsets; Figures 2 and 3a) and is interpreted as the roof of an axial magma chamber (AMC) [*Singh et al.*, 2006]. Dipping reflectors that may correspond to faults are observed at all offsets (Figure 3), except for a dipping event that we interpret as the western bounding fault, which is only observed at offsets >2500 m and seen on Figures 3b and 3c (the 2500 m threshold was observed on partial stacks with different offset ranges than the ones shown on Figure 3). Turning rays from within seismic layers 2A and 2B are observed at offsets >1500 m. An event is observed arriving in the farthest offsets (>4400 m), between 3.5 and 4 s, at times close to the AMC arrival time (Figure 3c), which is more continuous than the AMC event stacking at near offsets. This far-offset energy simulates the shape of layer 2A and extends across the axial valley. Ray modeling shows that this event could correspond to a multiple of layer 2A that is reflected down at the seafloor interface.

Refracted arrivals from layer 2A have very high amplitude (comparable to that of the seafloor; Figure 2) and can mask upper crust events. In order to properly image true reflection events in the upper crust as well as refracted energy coming from the base of layer 2A, we processed the data twice. The first set of processing was optimized to image layer 2A, with all offsets included in the stack and with a constant NMO velocity of 1900 m/s in the upper crust throughout the survey area. Since layer 2A arrival time on stacked sections is highly dependent on NMO velocity [*Harding et al.*, 1993], the use of a constant NMO

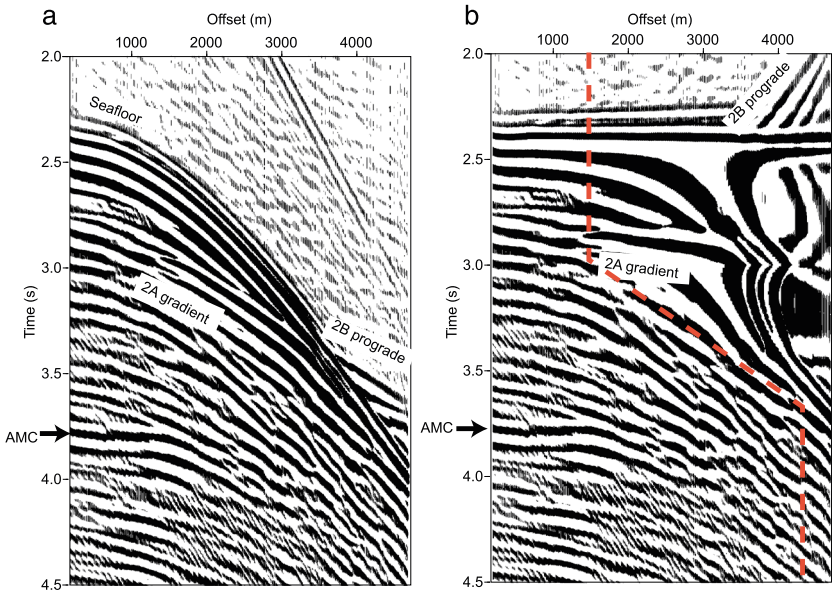

Figure 2. (a) SuperCMP gather located on the volcano (line 01, crossline number 1416–1517, CDP 4441–4542). (b) Same supergather after NMO correction with a velocity derived from velocity analysis. A first processing set was performed with all offsets included in the stack. A second processing set was performed with including in the stack only the energy to the left of the mute function (red dashed line); this allowed to image upper crust events otherwise masked by layer 2A arrivals. Note that the CMP gather contains hyperbolae that have a strong moveout even at late times; they come from energy diffracted at the seafloor and do not stack coherently.

velocity for layer 2A avoided artificial variations in layer 2A thickness due to local velocity picking errors. In the second set of processing, a mute function was applied before stack to suppress refracted energy: offsets $>$1500 m were muted from the seafloor to layer 2A time; at greater times, greater offset ranges up to 4300 m were progressively included in the stack. This mute function (shown in Figure 2b) allowed us to reveal shallow reflectors in the upper crust that were otherwise masked by strong layer 2A refracted arrivals.

4.2. Interpolation

The 100 m trace spacing in the crossline direction causes spatial aliasing of dipping events (including dipping branches of diffraction hyperbola) within the frequency range of our seismic signal. These spatially aliased dipping events cannot be properly migrated. Spatial aliasing can be avoided by reducing trace spacing using trace interpolation. The initial 100 m spatial sampling in the crossline direction was reduced to 25 m by trace interpolation after stack, allowing dips up to 50°/70° in the crossline direction at the seafloor/in the crust, respectively, to be unaliased at 20 Hz, and therefore properly imaged by migration. A dip-consistent trace interpolation was performed, based on the local slant stack technique of *Lu* [1985] using dip scans and semblance scaling. This technique consists in computing the semblance along a given number of dips across a window centered on the output sample location. For every dip, an amplitude is interpolated from the amplitudes of the two central traces to the output trace location. The amplitudes are then scaled by the corresponding semblances, summed, normalized (divided by the number of dips), and output as the interpolated sample. Because of computational limitations, we had to increase the CMP spacing along inlines from 6.25 m to 25 m before migration with a 3-D velocity model, which resulted in a data volume with a CMP spacing of 25 m in both directions.

4.3. Imaging

For all of the images presented in this paper, 3-D migration was performed using a finite difference algorithm with a two-pass approach, where the volume is first migrated in the inline direction and then in the crossline direction. Three-dimensional migration provides an accurate image of reflectors in areas of complex topography, which cannot be achieved by 2-D migration. This is particularly obvious on the seafloor reflector (Figure 4) where crossline migration performed during the second pass of 3-D migration effectively removes

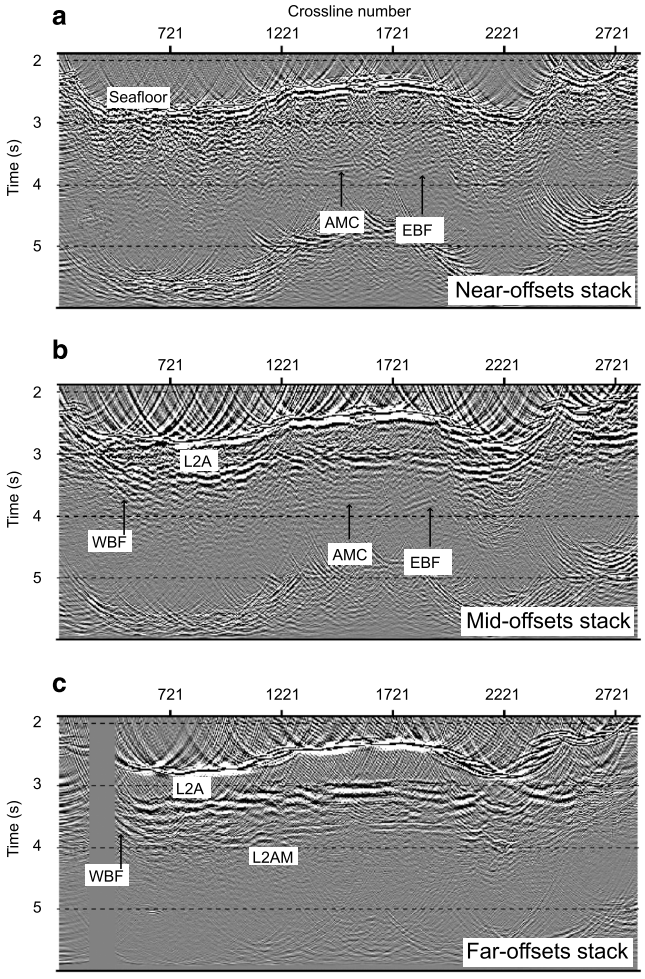

Figure 3. Partial stacks of line 7 including selected ranges of offsets (NMO was performed with a velocity derived from velocity analysis and the stacks were migrated at 1500 m/s for clarity): (a) near-offset (185–1500 m) stack, (b) midoffset (1500–3500 m) stack, and (c) far-offset (3500–4675 m) stack. Layer 2A energy is observed at offsets >1500 m. Between 3.5 and 4 s, an event that is present only at far offsets follows the shape of layer 2A. Ray-based travel time modeling shows that it could correspond to an intracrustal multiple of layer 2A (L2AM). See Figure 12b for profile localization.

out-of-plane energy coming from the crossline direction. Migration was performed using a velocity model derived from the SISMOMAR 3-D refraction study [*Seher et al.*, 2010b], as this velocity model gave similar but overall better results than models derived from migration velocity tests. For example, Figure 5 shows that the velocity derived from the 3-D refraction study best migrates the AMC reflector. Migration with realistic subcrustal velocities correctly collapses diffraction hyperbolae and therefore gives the real dimensions of the AMC and moves dipping reflectors updip to their subsurface location.

The time-migrated volume was then "vertically" converted to depth using the velocities derived from the 3-D refraction study [*Seher et al.*, 2010b]. The resulting depth image, which is a vertically stretched image of the time-migrated section, provides an estimation of the depth and geometry of each reflector, which is sensitive to velocity errors. The poststack migrated seismic cube is shown in depth domain in Figure 6.

4.4. Accuracy of Final Seismic Images

We constructed a map of seafloor bathymetry using picks of the seafloor arrivals on the seismic volume (Figure 7). Our map agrees well with the multibeam bathymetry (the mean of absolute differences between the two bathymetries is 10 m), which indicates that our results are accurate in terms of positioning at least for near offsets and that the 3-D processing is accurate as far as the seafloor reflector is concerned. The vertical uncertainty of our depth converted images varies from a few meters at the seafloor to ~300 m at the depth of the magma chamber, taking into account uncertainty in the velocity used for depth conversion. The horizontal uncertainty varies from a few meters at the seafloor to a few hundred meters at the depth of the magma chamber, given the fact that on time-migrated images, reflectors placed under dipping seafloor topography may be laterally displaced from their true subsurface location [*Black and Brzostowski*, 1994].

5. Results

5.1. Bathymetric Map From 3-D Seismic Reflection Data

Bathymetric maps of higher resolution than those of ship-board multibeam data can be obtained by extracting seafloor arrival times from migrated 3-D seismic reflection data [*Combier*, 2007; *Combier et al.*, 2008], owing to the denser spatial sampling (6.25 m) along the shooting direction achieved during multichannel seismic surveys compared to ship-board multibeam surveys. An estimate of the horizontal resolution of multibeam systems is given by the vertical beam footprint dimension, which was 50–60 m across track and 100–120 m along track at water depths of 1600–2000 m for the EM12D system used during the SISMOMAR cruise.

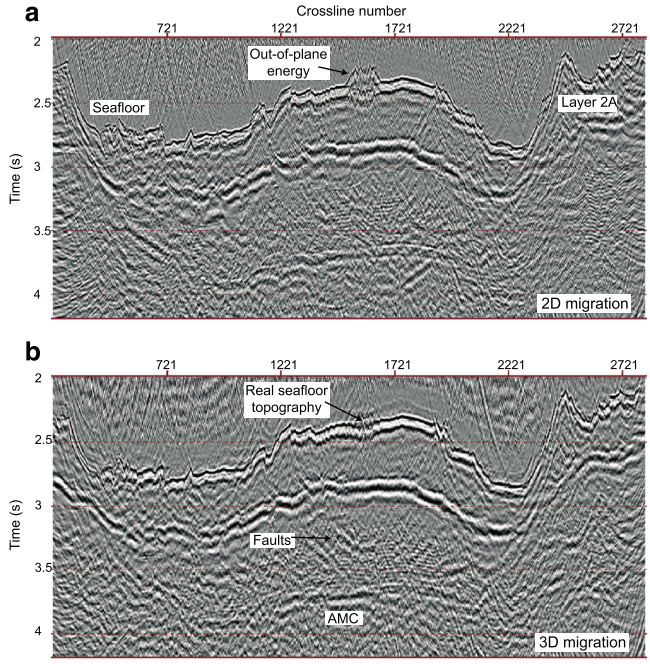

Figure 4. Comparison of migration in (a) 2-D and (b) 3-D and its effects on seafloor reflector geometry. Line 7 is represented, with both migrations performed at 1500 m/s with a frequency-wave number algorithm. The 3-D migration allows to effectively migrate energy coming from the cross-line dimension. Indeed, the image of a volcanic cone situated in the vicinity of line 7 (see Figure 12b for location of line 7) appears on the 2-D migrated line, but not on the 3-D migrated line. Moreover, real events are brighter after 3-D migration because their signal-to-noise ratio is increased by the summation performed during cross-line migration compared to inline migration only.

In order to be conservative in describing our seismic data quality, we will distinguish between "resolution" and "detection." Resolution means the ability to distinguish two features from one another, and detection means the ability to distinguish that some feature exists; the resolution limit is obviously always larger than the detection limit. The detection limit at the seafloor is the CMP spacing, which is 6.25 m for our 3-D survey in the across-axis direction. Horizontal resolution of seismic data can be estimated by taking into account the effects of spatial sampling, the migration operator and the positioning uncertainty. First, the horizontal resolution is limited by the spatial Nyquist wave number (i.e., twice the CMP spacing), which was 12.5 m along track (inline) and 200 m across track (crossline). Second, the horizontal resolution of seismic data, which can be defined on stacked sections by the width of the Fresnel zone, is improved by the process of migration [e.g., *Chen and Schuster*, 1999]. After poststack migration, the horizontal resolution Δx of seismic data can be approximated as [*Chen and Schuster*, 1999] $\Delta x = \lambda Z/L$, where λ is the dominant wavelength, Z is the depth of the target, and L is the survey migration aperture width. For a dominant frequency of 30 Hz ($\lambda = 50$ m), a water depth approximated to 1.8 km and a migration aperture width of 7 km at the Lucky Strike volcano, $\Delta x = 13$ m in the shooting direction. The positioning uncertainty of the first trace is 10 m [*Combier*, 2007]. The overall resolution of our seismic derived bathymetry is the geometric mean of the individual uncertainties: 21 m in the inline direction. In the crossline direction, the resolution is 200 m (twice the CMP spacing).

The seafloor arrival was picked on the time-migrated volume gridded at 6.25 m inline and 25 m crossline (this is different from the rest of the data set, which was picked at 25×25 m). We picked the first high-amplitude positive arrival, both manually and using an automatic detection utility based on waveform correlation. The seafloor arrival times were then converted to depth using a velocity (1493 m/s) and a constant shift (-20 m) that were determined by least squares fitting the arrival times with the EM12D multibeam bathymetry. The average absolute difference between the two bathymetric grids is of 10 m, with a standard deviation of 10 m. The resulting bathymetric map is shown in Figure 7a. Comparison with bathymetric maps from the onboard EM12D and deep-towed DSL-120 [*Scheirer et al.*, 2000] systems shows that our seismic bathymetry gives accurate results, except at the borders of the 3-D survey area due to errors in migration (maps available in *Combier* [2007]). For example, on the northern border of our bathymetric map, where the topography of the volcano is 3-D (with slopes dipping to the north), the seafloor arrival was hardly identifiable on the seismic image because of the out-of-plane seafloor scattering effect.

5.2. Dipping Reflectors and Faults

5.2.1. Faults on the Seafloor

We produced a tectonic sketch (Figure 7b) by interpreting our seismic-derived bathymetric map along with bathymetric gradient maps and profiles extracted from this map. An exponential transform was applied to the gradient map, and fault scarps were identified as the linear features whose slope is >90% of the

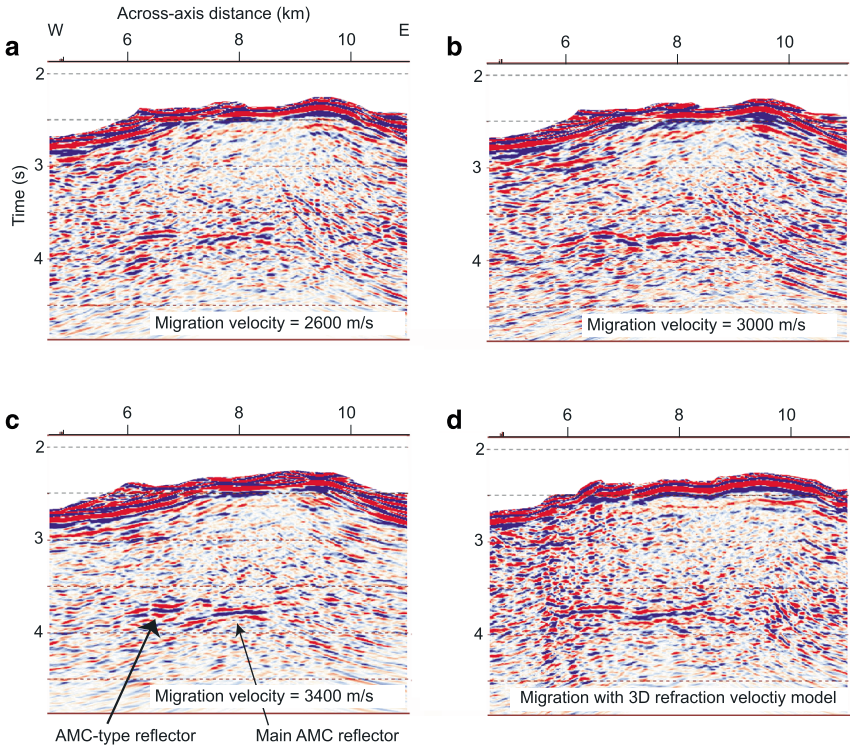

Figure 5. Close-up on the AMC reflector of seismic line 5 with four different migration velocities. Migration was performed in 3-D with a finite difference algorithm. (a–c) Migration is performed with a constant migration velocity of 2600 m/s, 3000 m/s, and 3400 m/s, respectively. (d) Migration is performed with the 3-D velocity model derived from travel time tomography [*Seher et al.*, 2010b]. Examination of the borders of the AMC reflector shows that it is undermigrated in Figure 5a (borders dip down), overmigrated in Figure 5c (borders dip up), but migrated at the correct velocity in Figures 5b and 5. Velocities derived from travel time tomography are thus suitable for migration. See Figure 12b for location of line 5.

largest slope. By order of decreasing importance (i.e., length of the fault and height of the scarp), the main faults in the survey zone (Figure 7b) are the two faults bounding the axial valley (>30 km long): the eastern bounding fault (EBF) and the western bounding fault (WBF), and four main faults dissecting the volcano: F1 and F1b, which appear to link at the north of our survey area (17 km long), F2 (15 km long) and F3 (10 km long). Other scarps of a few kilometers in length are present on the volcano and on the axial valley flanks. The eastern flank of the volcano is notable for an absence of scarps.

5.2.2. Faults at Depth

The major faults identified on the seafloor (Figure 7) are also observed at depth in the seismic sections, except faults F2 and F3.

Two dipping strong events are identified at depth in the seismic sections whose geometry suggests that they are the continuity at depth of the EBF and WBF observed on the seafloor (Figure 8). The EBF is a strong reflector that is imaged in the whole 3-D box. It is observed from 1.5 km below the seafloor (bsf) down to 3.8 km bsf, with a dip of 50 ± 3°. By contrast, the axial valley eastern wall (the footwall of the EBF) has a dip of 28–36° (dip calculated on profiles extracted from the multibeam bathymetry,

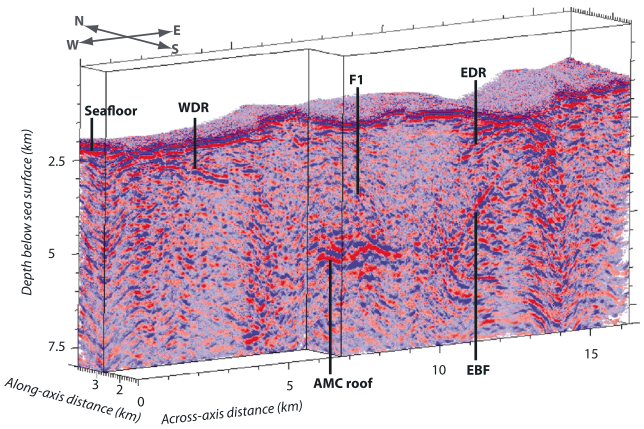

Figure 6. The 3-D view of the Lucky Strike volcano seismic reflectivity. Depth-converted poststack-migrated 3-D seismic cube. AMC melt lens, faults, and shallow-dipping reflectors in the upper crust are observed.

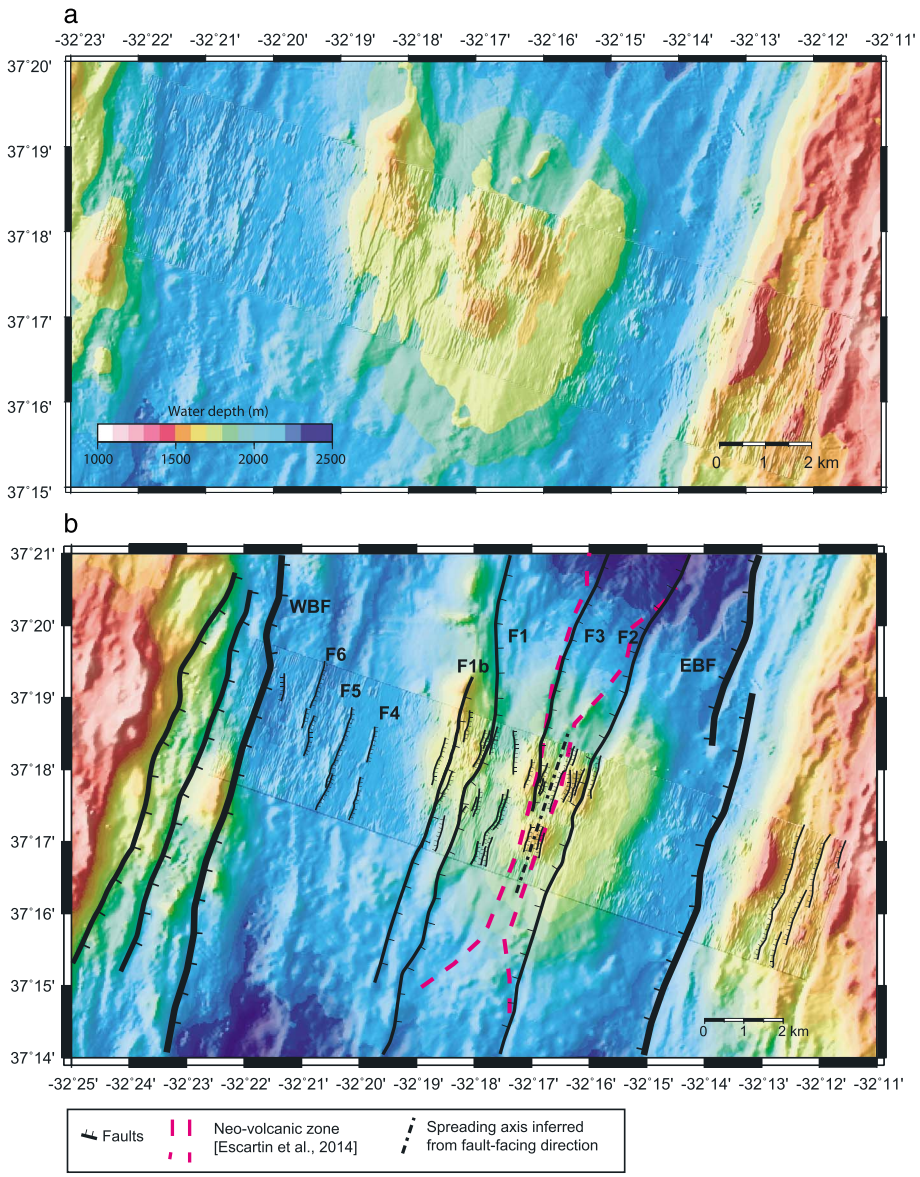

Figure 7. Seismic derived bathymetric map and structural sketch of the Lucky Strike volcano. (a) Seismic derived bathymetric map overlain on the multibeam bathymetry (Kongsberg Simrad EM12 Dual system, data from the SISMOMAR cruise). Gridding is at 5 m, and illumination is from the direction N289°E. (b) Structural sketch of the Lucky Strike volcano. Faults marked EBF, WBF, F1, F1b, and F5 are observed at depth on the seismic section.

away from zones where major collapse features are inferred). The fact that the scarp on the seafloor has a shallower dip than that at depth may be explained by elastic rebound of the footwall after exhumation and by the presence of collapse features. The EBF is observed reaching depths ~0.5 km deeper than the AMC roof, but at a distance of 1.5 km from the AMC (Figure 8a); the EBF is not observed directly below the AMC reflector.

The dipping reflector we interpret as the WBF is observed only at far offsets (offsets $>$ 2500 m; Figure 8b). It is visible from 1.5 km bsf to 2.0 km bsf, with a dip of $33 \pm 5°$ at depth. The WBF is observed reaching a depth ~1 km above the AMC, 4 km away from the AMC. Since it is observed only at far offsets, the depth of the event on a stacked section is highly dependent on stacking velocity; the depth of the event is thus constrained with an uncertainty of a few hundred meters. On the seafloor, the western bounding wall of the axial valley is actually composed of three major scarps (Figures 7b and 1). These three scarps appear to link at depth in a single fault damage zone that constitutes the WBF reflector.

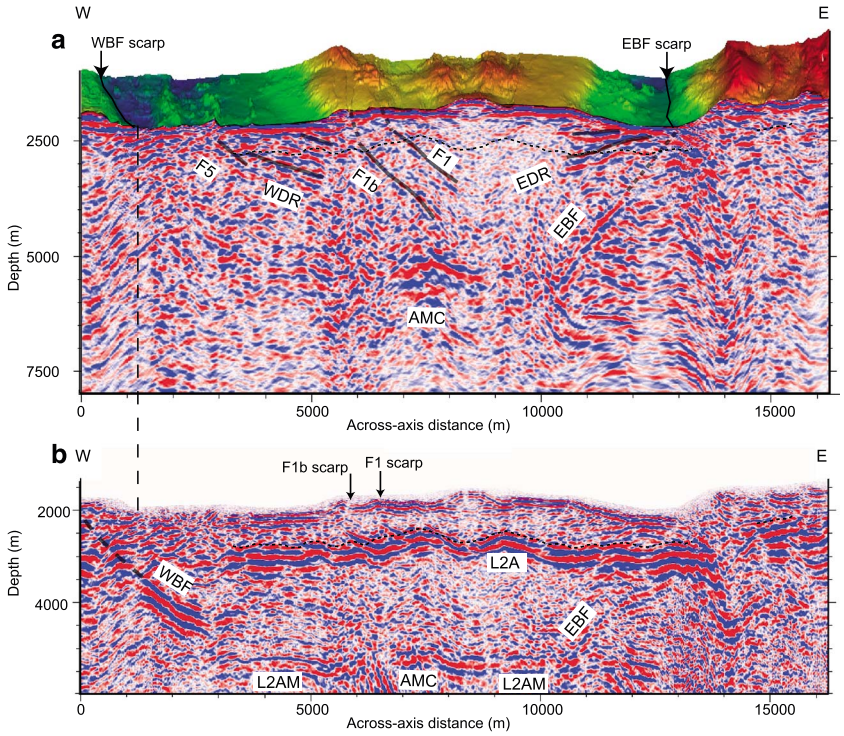

Figure 8. Seismic line 13 showing faults observed at depth on the Lucky Strike volcano. (a) Depth converted profile with far offsets muted. (b) Depth converted profile with all offsets included in the stack. The layer 2A reflector as picked in Figure 8b is shown as a black dashed line. Layer 2A (L2A) is visible (picks in black dashed line), along with its intracrustal multiple (L2AM). EBF/WBF: eastern/western axial valley bounding fault, EDR/WDR: eastern/western dipping reflectors. See Figure 12b for location of line 13. Depth conversion was performed with velocities derived from 3-D travel time tomography [*Seher et al.*, 2010b]. Vertical exaggeration 1:1.

A set of major faults is also observed at depth beneath the volcano. Two dipping reflectors seem to be the continuity in depth of the faults F1 and F1b identified on the bathymetry (Figures 8 and 9). Although they are visible at near offsets (Figure 8a), they are often brighter when far offsets are included in the stack. F1 is visible at depth throughout most of the survey area, whereas F1b disappears in the north. Both F1 and F1b have a dip of 45 ± 5° at depth. They are not imaged in the first 500 m of the crust, where a steeper dip of 50–60° is required to link the reflectors with the seafloor scarps (Figure 8a). Both F1 and F1b are observed over lengths of 2–3.5 km. F1b reaches a depth of 2.5 km bsf, just 0.7 km above the AMC. F1 reaches a depth ~1.4 km above the AMC. A dipping reflector is imaged on the western side of the axial valley that seems to correspond to scarp F5 identified on the seafloor (Figure 8). It has a dip of 37° and is observed down to 800 m bsf.

Three of the five major faults imaged at depth in our seismic sections have dips of 45–50° (the EBF dips 50 ± 3°, F1 and F1b dip 45 ± 5°); the WBF dips 33 ± 5°, and F5 dips 37°. The dips of the faults observed at depth in the seismic image at Lucky Strike are consistent with the moderate dips of 30–60° inferred from earthquake focal mechanisms at mid-ocean ridges [*Toomey et al.*, 1985; *Huang and Solomon*, 1988; *Thatcher and Hill*, 1995]. Fault dips at the seafloor ranging from 30° to 80° have been observed from submersibles [e.g., *Karson et al.*, 1987; *Mével et al.*, 1991]. Seismic reflection profiles at the Reykjanes Ridge [*Peirce et al.*, 2007] show reflectors dipping ~55° at depth, which can be traced to scarps within the axial valley walls.

5.2.3. Fault Facing Direction

The structural sketch (Figure 7b) and seismic sections (Figure 8) show two distinct domains: a domain where faults dip mostly eastward and another domain where faults dip mostly westward. The limit between these two domains is relatively sharp and would be represented by an imaginary line passing through the center of the circular depression between the three cones on the volcano and orthogonal to spreading. This boundary between fault-facing directions is defined within a width of 200–500 m. It is located within the neovolcanic

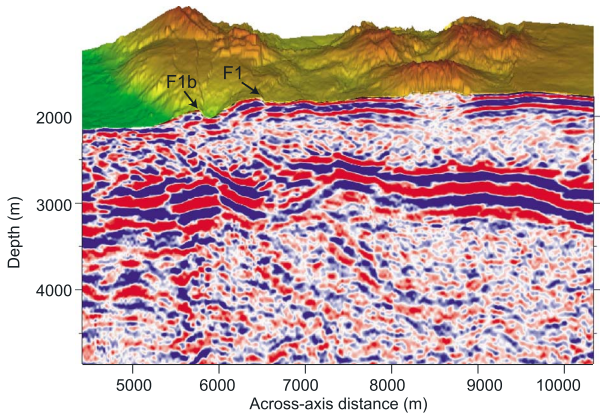

Figure 9. Close-up (line 8) on dipping reflectors observed at depth on the Lucky Strike volcano and associated faults on the seafloor. Dipping reflectors in the seismics may correspond to faults F1 and F1b observed on the seafloor. See Figure 12b for location of the section.

zone determined by *Escartín et al.* [2014] from interpretation of seafloor texture on side scan sonar data. It is also consistent (within ~200 m accuracy) with the location of the linear high magnetization anomaly identified by *Miranda et al.* [2005], which is commonly interpreted as the neovolcanic axis.

5.2.4. Shallow Dipping Reflectors

A set of reflectors dipping toward the axis is observed in the upper crust beneath the western and eastern flanks of the volcano; they are marked western dipping reflectors (WDR) and eastern dipping reflectors (EDR) in Figure 8a and are also shown in Figure 10. These reflectors seem to be arranged in a fan-like structure, with deeper reflectors having higher dips than shallower reflectors. On the western flank, the WDR are observed from the near-seafloor level down to 1 km bsf. The deeper reflector has a dip of $18 \pm 4°$ whereas the shallower reflectors have dips of 2–8°. On the eastern side, the EDR are observed from the near-seafloor level down to 1 km bsf. The deeper reflector has a dip of $16 \pm 2°$ whereas the shallower reflectors have dips of ~3°. These reflectors are generally masked by the layer 2A turning ray arrivals on images where layer 2A has not been muted (Figure 8b).

It is difficult to interpret these reflectors as faults because the shallowest reflectors, while reaching the vicinity of the seafloor, are subhorizontal (3°–8°dips; Figure 10). Such shallow dips cannot correspond to active normal faults: low angle normal faults, with dips $<30°$ such as detachment faults, do occur in oceanic crust, but are associated with large amounts of extension (>1 km) [*Forsyth*, 1992]. Moreover, most of these reflectors cannot be linked to any visible scarp on the seafloor. They are therefore unlikely to be faults; instead, they may correspond to lithological alteration or porosity boundaries such as successive lava flow units that have subsided.

5.3. The Layer 2A Event

The layer 2A event is present throughout the study area. Because layer 2A arrivals are turning rays arriving at far offsets, the travel time to layer 2A arrivals on seismic sections is highly dependent on the NMO velocity [*Combier*, 2007; *Seher et al.*, 2010c]. By changing the NMO velocity from 1800 to 2000 m/s, layer 2A thickens by ~120 ms at the same CMP on a stacked section. We used a velocity of 1900 m/s for NMO, and therefore, we estimate a 60 ms uncertainty in layer 2A two-way time due to NMO velocity uncertainty and 25 ms picking uncertainty (a quarter of the dominant wavelength) which gives a total uncertainty in layer

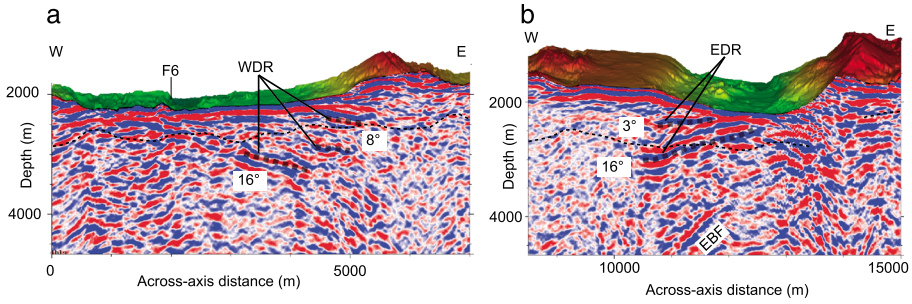

Figure 10. Close-up on shallow-dipping reflectors WDR and EDR. The sections were depth converted. (a) Close-up on the western flank of the volcano (line 31). (b) Close-up on the eastern flank of the volcano (line 12). WDR and EDR are marked by a thick dashed line, and layer 2A is marked by a thin dashed line. See Figure 12b for location of the sections.

2A two-way time of 85 ms, corresponding to ~110 m at 2500 m/s. We must add a 150 m uncertainty due to the 3-D upper crust velocity model we used for depth conversion, because it is poorly constrained within layer 2A due to the absence of clear prograde layer 2A arrivals [*Seher et al.*, 2010c]. Layer 2A depth in our study is therefore given with a total uncertainty of ~200 m (i.e., square root of the sum of square uncertainties). Since a constant velocity was used to stack layer 2A, the relative thickness of layer 2A throughout the survey area presented in this study is better constrained than the absolute thickness.

A map of layer 2A thickness is shown in Figure 11a. The pattern of variations in layer 2A thickness is similar to the pattern of travel time variations observed between the seafloor and layer 2A (map available in *Combier* [2007]). The layer 2A thickness map shows three domains: a domain where layer 2A is $>900 \pm 200$ m thick, which corresponds to the volcano and to some regions to the west of the volcano; a domain where layer 2A is within $500–700 \pm 200$ m thick, which corresponds to off-axis areas; and a third domain, which consists in lineated zones that are found on the volcano and off-axis, where layer 2A is the thinnest ($<400 \pm 200$ m thick).

5.4. The AMC Reflector

The AMC reflector was picked on the depth converted volume, both manually and using an automatic detection utility based on waveform correlation. The AMC reflector has a reverse polarity compared to that of the seafloor, indicating a decrease in velocity and/or density below the reflector. We picked the first negative amplitude arrival of the AMC event. The across-axis width of the AMC is maximum (2 km) beneath the center of the volcano and reduces to 1 km toward the northern and southern borders of the survey zone (Figure 12). The along-axis extent of the AMC reflector cannot be determined by our study since the AMC extends beyond our survey area. A profile that was shot along axis shows that the AMC length is <7 km [*Singh et al.*, 2006].

The topography of the AMC in time and depth is shown on Figure 13; it should be noted that only large-scale variations in the topography of the AMC are properly estimated by our study. Indeed, unlike fast spreading ridges where the topography is smooth (a few tens of meters topography on the ridge summit), the rough seafloor topography above the AMC reflector (a few hundred meters) at Lucky Strike causes curving of raypaths, which is not taken into account in our depth conversion process which assumes that zero-offset rays travel vertically (depth migration would provide a more accurate image of the AMC); this can lead to a few hundred meters of inaccuracy in both the lateral and vertical positioning of the AMC. Moreover, while uncertainties in stacking velocity and picking produce negligible (<0.07 km) errors in the AMC depth, an uncertainty of 0.3 km/s in the mean upper crustal velocity used for depth conversion maps into an ~0.2 km uncertainty in the AMC depth. Consequently, the position and depth of the AMC are given here within a few hundred meters accuracy. Given these restrictions, general conclusions can be drawn from Figure 13: the AMC depth varies between 3.0 and 3.8 km bsf, with a mean depth of 3.5 km bsf. The AMC reflector overall shallows by ~0.2 km in the center of our survey area (where the AMC is ~3.3 km bsf) compared to the northern and southern borders (where the AMC is ~3.5 km bsf). The AMC is also the widest in the center of our survey area. The AMC therefore has the shape of an elongated dome which is shallowest beneath the central part of the volcano.

A subhorizontal reflector slightly shallower than the AMC level is visible 300 m west of the AMC reflector on lines 4 to 13. It is disconnected from the AMC reflector at high migration velocities (Figure 5c). The contours of this AMC-like reflector are mapped on Figure 12.

6. Discussion

6.1. Implications of the Presence of a Melt Body at a Slow-Spreading Ridge

6.1.1. Thermal Structure

Evidence that the AMC reflector is associated with hot material is provided both by the polarity of the reflector, which indicates a decrease in velocity and/or density below the reflector, and by tomography results that show a low-velocity zone centered at ~3.5 km depth beneath the volcano [*Seher et al.*, 2010a]. The location, dimensions (<7 km long [*Singh et al.*, 2006], 2 km wide beneath the volcano center), and shape (dome-shape shallowing beneath the volcano center) of the AMC reflector at Lucky Strike suggest that strong focusing of melt occurs at the segment center. By contrast, at fast spreading ridges,

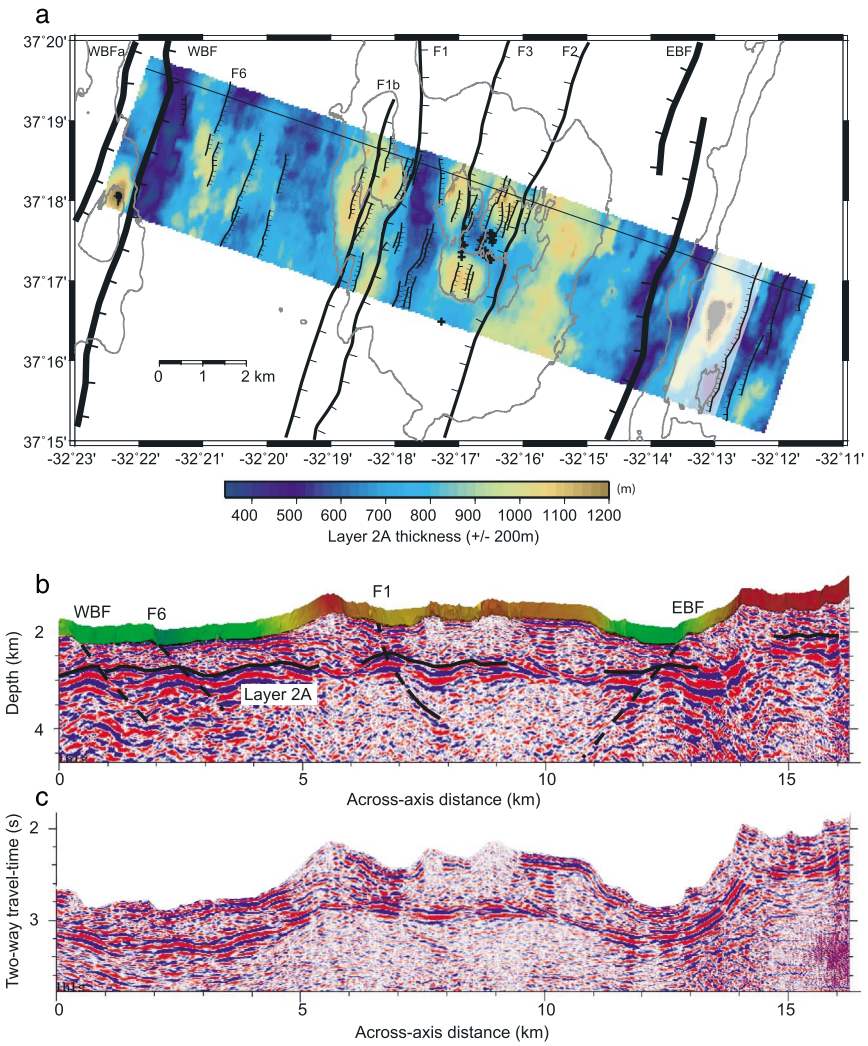

Figure 11. Layer 2A thickness variations. (a) Map of layer 2A thickness with the structural sketch of Figure 7b and bathymetric contours 1700 m and 1900 m overlain. We picked the first high-amplitude event in the layer 2A wavelet throughout the depth converted volume (depth conversion with velocities from the 3-D refraction study of *Seher et al.* [2010b]) and subtracted the seafloor depth to obtain layer 2A thickness. A white transparent mask is overlain on zones where layer 2A arrivals could not be identified with confidence and correspond to steep slopes of the seafloor. (b) Depth converted, time-migrated seismic line 35. (c) Time-migrated line 35.

the AMC reflector is observed continuously beneath ridge segments, over lengths of 50–100 km with a width usually $<$ 1 km [*Hooft et al.*, 1997].

The Lucky Strike segment has an overall morphology typical of slow spreading ridges, as attested by the presence of a well-developed median valley that implies a thick lithosphere [*Tapponnier and Francheteau*, 1978; *Chen and Morgan*, 1990]. The recording of earthquakes in very close proximity to the AMC during the SISMOMAR experiment [*Dusunur et al.*, 2009] also suggest that the Lucky Strike magma chamber is surrounded by cold crust, with isotherms that steeply slope around the AMC both along axis and across axis [*Dusunur et al.*, 2009].

6.1.2. Magma Chamber Steady State or Ephemeral?

Classical thermal models that assume a standard melt supply (i.e., a melt supply that produces a 6 km thick crust, with a 2-D geometry invariant in the along-axis direction) predict that the crust at slow spreading ridges is too cold to hold a steady state melt body [*Phipps Morgan and Chen*, 1993; *Chen and Lin*, 2004]. However, the AMC at Lucky Strike may exist longer than predicted by thermal models because there appears to be efficient melt focusing at the Lucky Strike segment center, as attested by the geometry of

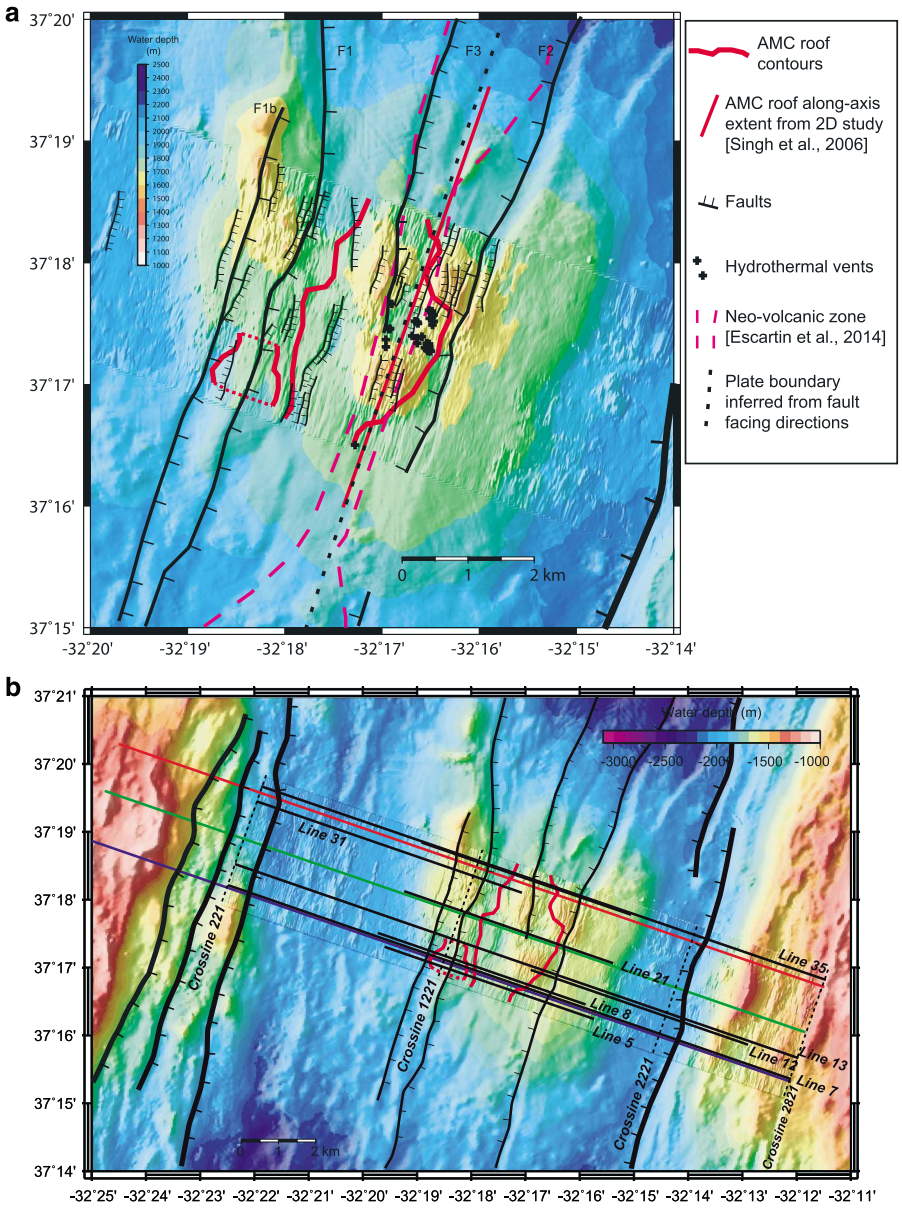

Figure 12. Magma chamber roof contours overlain on bathymetry. (a) Close-up on the volcano. Seismic derived bathymetric map is overlain on the multibeam bathymetry (Kongsberg Simrad EM12 Dual system, data from the SISMOMAR cruise). Gridding is at 5 m, and illumination is from the direction N289°E. Faults from Figure 7 are reported. (b) Magma chamber contours and localization of profiles shown in the paper. The red, green, and blue lines are profiles along which cumulative fault heaves have been computed (Figure 14).

the magma chamber and the crustal thickening from ~6 km at the segment ends to ~7.5 km at the segment center [*Seher et al.*, 2010a]. This melt focusing probably yields a hotter crust at the segment center than that predicted by classical thermal models where the melt supply is invariant in the along axis direction.

Dusunur [2008] ran analytical and numerical simulations of the Lucky Strike thermal structure, taking into account an increased melt supply and/or melt focusing, along with the geometrical constraints on the magma chamber derived from our seismic experiment. These simulations indicate that in the absence of replenishment, the Lucky Strike magma chamber cooling time may range from a few thousands to a few tens of thousands of years.

The AMC-like reflector observed 300 m to the west of the AMC reflector in the south of the survey area (Figures 5c and 12) may correspond to a small secondary melt sill emplaced in the vicinity of the main AMC melt sill. This secondary sill is probably ephemeral.

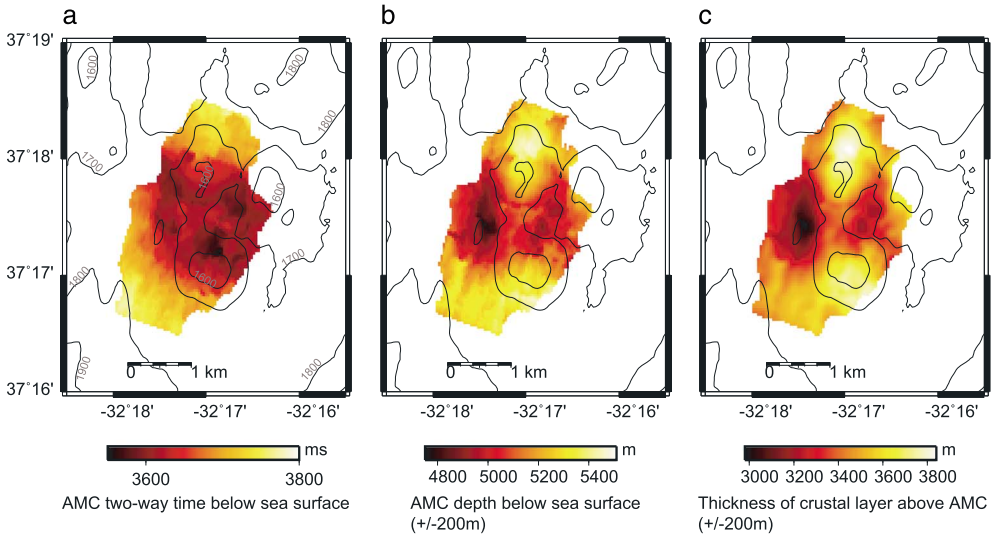

Figure 13. AMC roof topography with bathymetric contours. Bathymetric contour interval is 100 m; bathymetric values are indicated along contours. (a) AMC roof in time below sea surface, (b) in-depth below sea surface, and (c) in-depth below seafloor. Depth conversion was done assuming vertical rays with velocities from the 3-D travel time tomography study [*Seher et al.*, 2010b]. Minimum-maximum values and mean values are, for each panel, 3550–3780 ms and 3660 ms (Figure 13a), 4.76–5.50 km and 5.17 km (Figure 13b), and (c) 2.98–3.84 km and 3.46 km (Figure 13c).

6.1.3. Cooling of the AMC

The top of the AMC is commonly interpreted to correspond to a thermal crystallization boundary [e.g., *Phipps Morgan and Chen*, 1993; *Hooft et al.*, 1997] rather than a neutral buoyancy level. *Crawford et al.* [2013] suggested that the present-day shape of the AMC roof, which is shallowest 1 km west of the neovolcanic axis (Figure 13c), may be the result of cooling by hydrothermal circulation being the most efficient on-axis, pushing down the AMC there more than elsewhere. This interpretation is supported by microseismicity measurements on the Lucky Strike volcano which showed most seismicity occurs along two microearthquake clusters beneath the most recent axial graben and southern cone; these events are interpreted as due to thermal contraction, mainly at the base of downgoing hydrothermal flow [*Crawford et al.*, 2013].

6.2. Volcanism in the Upper Crust

6.2.1. Thickness of the Lavas Section

We interpret the shallow-dipping reflectors observed beneath the volcano flanks down to 1 km bsf, EDR and WDR, as lithologic boundaries such as successive lava flows, which are now dipping toward the axis as the result of subsidence. *Arnulf et al.* [2012, 2014] have identified very shallow reflectors they also interpret as possible volcanic sequences, at very shallow depths (<150 m bsf) beneath the Lucky Strike volcano. These very shallow reflectors are not identifiable in our study as we have lower vertical resolution than the one obtained by *Arnulf et al.* [2012, 2014] using downward continuation. Reflectors such as EDR and WDR beneath the volcano flanks are not imaged by their study as they are masked by layer 2A refracted arrivals. In our study, WDR and EDR are only observed beneath the volcano flanks and not in the axial part (area between 5.7 km and 10.5 km in Figure 8a). This is likely due to the fact that in the axial area, buried lava flows would be crosscut by a lot more dykes and faults than in the less active volcano flanks areas, destroying the continuity of lava flow reflectors.

If our interpretation of WDR and EDR as lava flow paleosurfaces is correct, the extrusive section can reach a thickness of at least 1 km on the volcano flanks (at the across-axis distance 4000 m in Figure 10a and 10500 m in Figure 10b). We note that the WDR are observed deeper than the picked base of layer 2A. However, as explained before, the stacking time of the layer 2A pseudoreflector is very sensitive to NMO velocity and there is therefore a large uncertainty in the depth of the layer 2A base; we therefore cannot constrain nor interpret the relative positions of the WDR and the base of layer 2A.

6.2.2. Geological Nature of Layer 2A

The oceanic crust is divided into seismic layers based on seismic velocities and velocity gradients, layer 2A and 2B being the first two igneous layers. In young oceanic crust (age $<$1–2 Ma), layer 2A is characterized by velocities in the range 2.2–2.8 km/s with a high-velocity gradient at its base, where velocities $>$4–5 km/s are reached in a few hundred meters [e.g., *Harding et al.*, 1989; *Christeson et al.*, 1994]. The gradient at the layer 2A/2B transition is presumably due to a reduction in porosity, but the underlying cause of this reduction is still the subject of debate: it could result from a transition in igneous rock type such as the lavas/sheeted dyke transition [e.g., *Harding et al.*, 1989, 1993; *Toomey et al.*, 1990; *Christeson et al.*, 1994; *Seher et al.*, 2010c; *Arnulf et al.*, 2014] or it could be related to physical or chemical mechanisms affecting porosity [e.g., *McClain et al.*, 1985; *Christeson et al.*, 2007].

Figure 11a shows that thick layer 2A is associated with volcanic topographic highs, e.g., the smooth eastern flank of the volcano, the volcanic ridge that composes the western flank of the volcano, and the three volcanic cones surrounding the lava lake. Figures 11a and 11b also show that elongated zones of thin layer 2A are associated with major faults (this is also observed by *Arnulf et al.* [2014]). The above two observations are consistent with a layer 2A horizon corresponding to the lavas/sheeted dykes transition, with lava sections thicker beneath volcanic highs and thinner (through tectonic thinning) near faults. However, we cannot discard the hypothesis stating that layer 2A marks another transition, such as an alteration front below which pores and cracks would be sealed by mineral crystallization as proposed by *Christeson et al.* [1994]. Pore closure with depth owing to confining pressure could create a pore diameter threshold at which cracks are easily sealed with alteration products. The thicker layer 2A beneath volcanic topographic highs could in this case be explained by a higher porosity causing a lower density and thus a deeper depth of pore closure. The layer 2A thinning associated with major faults could be explained, as before, by tectonic thinning of the porous layer. It could also be related to a porosity reduction due to faults in the highly porous upper crust: through grain size reduction in the fault core and through mineral precipitation due to enhanced fluid circulation along and around the fault (e.g., during fault activity).

6.3. Tectonic Deformation

6.3.1. Faults as Seismic Reflectors in the Oceanic Crust

Faults are ubiquitous at mid-ocean ridges according to seafloor observations, yet very few faults are imaged in seismic data, in part due to the rough basaltic seafloor surface that scatters energy throughout the section [*Mutter and Karson*, 1992]. Still, some dipping reflectors interpreted as faults have been identified on old oceanic lithosphere [e.g., *Mutter and Karson*, 1992; *Morris et al.*, 1993; *Salisbury and Keen*, 1993; *Reston et al.*, 1996; *Singh et al.*, 2007] and at mid-ocean ridges: *Mutter and Karson* [1992] interpreted shallow-dipping along-axis reflectors in the Mark area of the MAR as detachment faults, and *Peirce et al.* [2007] identified ~55° dipping reflectors that can be traced to scarps within the axial valley walls of the Reykjanes Ridge. By linking fault scarps on the seafloor with fault reflectors at depth, our study allows us to discuss why and when faults can be observed in the seismic section.

Fault zones are composed of distinct components: a fault core where most of the displacement is accommodated and an associated damage zone that is mechanically related to the growth of the fault zone [e.g., *Caine et al.*, 1996]. Grain-size reduction and/or mineral precipitation generally yield fault cores with lower porosity and permeability than the adjacent protolith. By contrast, in the fault damage zone, porosity and permeability may be enhanced relative to the core and the undeformed protolith [e.g., *Goddard and Evans*, 1995]. Wide damage zones may indicate multiple episodes of slip and the overprinting of successive deformation events [*Caine et al.*, 1996].

The impedance contrast within faults that are imaged by seismic reflections may be caused by modifications in porosity associated with the fault core or damage zone. It may also reflect a discordant contact between two lithological units (e.g., gabbros in contact with lavas), as is probably the case for the axial valley bounding faults whose large throw ($>$500–800 m) is likely to produce discordant contacts over significant lengths of the fault plane.

The upper part of the crust at mid-ocean ridges is likely to have a high porosity as shown by geological observations of lavas (e.g., large voids between pillows in pillow lavas) and by the low seismic velocities of layer 2A. In the highly porous upper crust, a fault may therefore represent an impedance contrast if

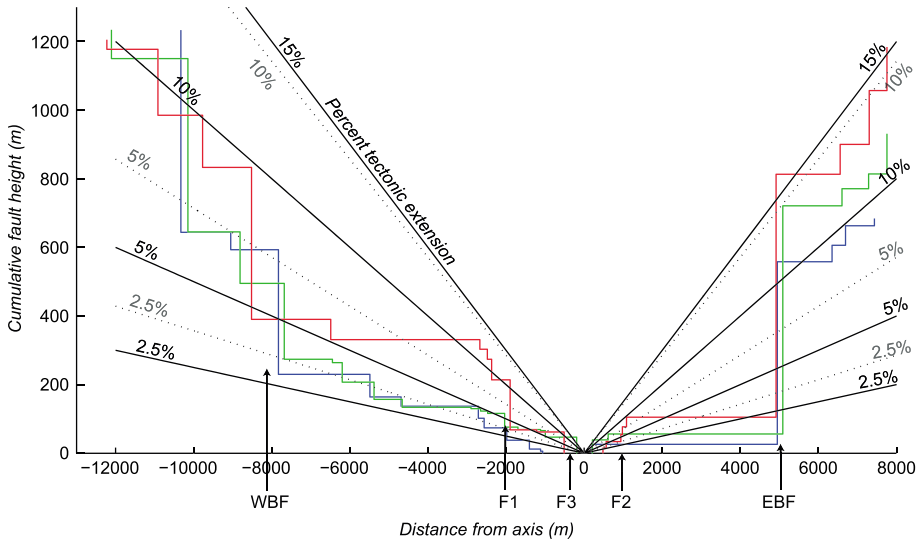

Figure 14. Cumulative fault scarp height as a function of distance from axis, along the three profiles plotted on Figure 12b. Black solid/grey dotted lines are percentage of tectonic extension over total plate extension, assuming 45%/55% fault dips, respectively.

its core hosts a significant enough reduction in porosity. In deeper levels of the crust where porosity is small, the visibility of a fault in seismic reflections may depend on the porosity increase associated with the fault damage zone. The fact that faults are hardly identifiable in the shallower part (the first 500 m) of the crust, but are better observed in deeper levels (Figures 8 and 9), may be due to the fact that faults are observable in our area only when the porosity of the surrounding rock is sufficiently reduced compared to the fault damage zone porosity. An alternative explanation could be that fault dips in the first 500 m of the crust are steeper than 70° and therefore are not imaged because of aliasing problems (frequencies $>$21 Hz are aliased for dips $>$ 70°, $\Delta x = 25$ m, and $v = 2000$ m/s; from equation giving f_{max} in paragraph 3).

Most reflectors that are observed in the seismic image (EBF, WBF, F1, and F1b) correspond to major scarps identified on the seafloor. This is consistent with both explanations for the impedance contrast linked with faults: they are the faults with the greatest throw and therefore the longest discordant surface, but they are also likely to have the widest associated damage zone. The detection limit of a planar heterogeneity is commonly within $\lambda \div 10$ and $\lambda \div 8$ depending on the noise level, λ being the dominant wavelength of the seismic wave. For the SISMOMAR survey where λ~120 m in the shallow crust and λ~325 m in the midcrust (at 3 km depth bsf), a fault damage zone would be imaged if it is wider than 15 m in the shallow crust and 40 m in the midcrust. The WBF is particular because it is only visible at far offsets (Figure 8b). This may be due to a very progressive damage within a wide damage zone, which would produce an impedance gradient rather than an impedance contrast.

6.3.2. Tectonic Extension

Tectonic extension through slip on faults accounts for at least 10% of the total plate extension (considering fault dips of 45°; Figure 14). This strain rate is similar to that observed near 29°N on the MAR and greater than that observed near 19°30′S on the superfast spreading southern East Pacific Rise, where the average tectonic strain is found to be ~11% and ~4% of the total plate extension, respectively [*Escartin et al.*, 1999; *Bohnenstiehl and Carbotte*, 2001]. Tectonic extension is visible mainly within 2.5 km of the axis along faults rifting the volcano (a few meters to 150 m vertical heave) and on the axial valley bounding faults (Figure 14). The EBF and WBF, with an apparent vertical heave of 600–800 m, represent 85% and 75% of the total vertical heave of axial valley faults to the east and west of the axis, respectively (Figure 14). The outer flanks of the volcano, with smooth seafloor textures, show no sign of active deformation, although ancient fault scarps may be buried under lava flows. These smooth seafloor textures to the west of fault F1 and to the east of fault F2 (Figure 7) suggest that an initial volcanic edifice has been rifted by faults F1 and F2 as proposed by *Escartín et al.* [2014].

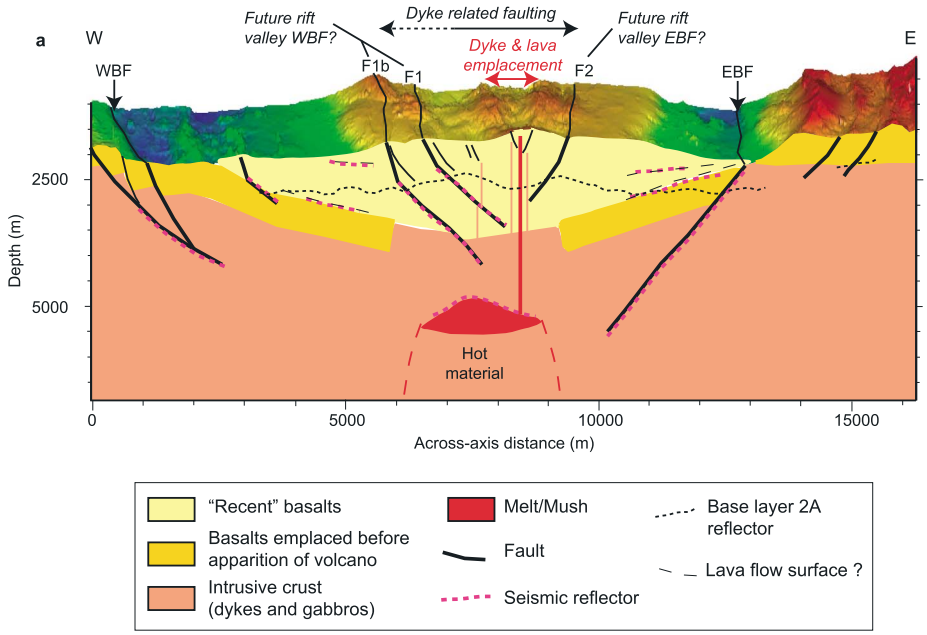

Figure 15. Interpretative sketch of the crustal structure beneath Lucky Strike volcano based on seismic observations. Sketch is based on seismic line 13 (Figure 8). If shallow-dipping reflectors WDR and EDR represent lava flow units as we suggest, the extrusive section can reach at least 1 km thick on the flanks of the volcano, by piling up and subsidence of successive lava flows erupted at the volcano.

6.4. Interplay Between Tectonics and Magmatism

6.4.1. Dyke-Associated Faults and Neovolcanic Axis Location

Studies conducted at slow spreading ridges and on their aging lithosphere have shown that nearly all faults mapped at slow spreading centers dip toward the axis [*Buck et al.*, 2005]. At a large scale, this is explained by the fact these faults result from stretching of thickening lithosphere [*Buck et al.*, 2005]. Faults present over the 2 km wide AMC, where the lithosphere has a constant thickness, also dip toward a single axis, indicating that another mechanism controls fault-dip orientation at a smaller scale. Normal faulting can be induced by dike emplacement as described by *Rubin* [1992], where normal and shear stress perturbation in the vicinity of a dyke that has not reached the surface is such that faults are more likely to develop with a dip facing toward the dyke [*Pollard and Segall*, 1987; *Rubin and Pollard*, 1988]. Considering such a mechanism, our results suggest that consecutive dyking events have occurred repeatedly in the same place, that is the 200–500 m wide zone delimiting the two fault-facing direction domains, which represents the plate boundary (Figure 12). If we assume that faults facing away from the axis have not all been buried under lava flows, we see no evidence for a recent shift in the spreading axis location. The western volcanic ridge where *Ondréas et al.* [1997] identified recent pillow lavas may only be an occasional magma exit where diking has not been frequent enough to control fault facing direction. The fact that shallow-dipping reflectors which likely represent subsiding lava flow units also dip toward the present-day spreading axis is a further indication that the spreading axis has remained in the same location throughout the construction of the volcano.

6.4.2. Evolution of the Lucky Strike Volcano

Our interpretation of the Lucky Strike volcano based on seismic observations is shown on Figure 15. Faults observed at Lucky Strike can be divided into two categories: superficial faults (throw up to a few tens of meters; they are not imaged at depth in the seismic and certainly reach less than 1 km depth) and deeply rooted faults (throw $>$100 m, most often imaged in the seismic reaching depths $>$1 km). Superficial faults are observed dissecting the seafloor in the region above the AMC and are likely related with dyke emplacement as discussed above. Deeply rooted faults are not many (EBF, WBF, F5, F1, F1b, and possibly F2) and are responsible for a significant part of the plate extension as shown on Figure 14. F1-F1b and F2 that rift the volcano seem to be presently constrained in depth by both the AMC presence and by their geometrical situation (F1 and F2 cannot cross each other). When the AMC cools down, or when plate spreading has rafted F1 and F2 far enough away from the AMC, F1 and F2 may become the new main axial valley bounding faults, replacing the EBF and WBF.

7. Conclusion

A full 3-D analysis of the seismic reflection structure of Lucky Strike volcano provides insights into the mechanisms of crustal accretion at the center of the Lucky Strike segment. The Lucky Strike segment shows a strong focusing of melt delivery at the segment center, which is occupied by a large volcano covered by a lava section reaching at least 1 km thick, as attested by shallow-dipping reflectors that we interpret as lava flow units. A magma chamber is present at 3.4 ± 0.4 km depth beneath the volcano; it is <7 km long and reaches a maximum width of 2 km at the center of the volcano. Major faults are observed at depth in the seismics, including the axial valley bounding faults and some of the faults that dissect the volcano. The fault reflector observed reaching the closest from the AMC is a fault that rifts the volcano (F1b), observed down to ~700 m above the AMC. Most melt extrusion through dyking from the magma chamber to the seafloor is focused within a narrow axis (width $<$ 500 m) that delimits two fault-facing domains (eastward and westward dipping) and that corresponds to the present-day plate boundary. This axis of extrusion seems to have remained stable throughout the construction of the volcano as suggested by fault-facing directions and the dip of reflectors we interpret as lava flow units. Magmatic production at the center of the segment is accompanied by synchronous faulting: tectonic extension through slip on faults accounts for at least 10% of the total plate extension.

Acknowledgments

The streamer geometry reconstruction method and the binning process are described in the supporting information. The SISMOMAR seismic data and the bathymetric map derived from the seafloor reflector are available upon request to Laboratoire de Géosciences Marines, IPGP, Paris, France. The INSU MOMAR program funded the acquisition of SISMOMAR project. We thank the captain (J.-R. Glehen) and the crew of the French research vessel Atalante for providing support during the SISMOMAR cruise and the seismic team of GENAVIR for acquiring the seismic data. We also thank members of the onboard scientific party Helene Carton, Juan Pablo Canales, and J. Miguel Miranda who helped make this project a success. We also thank Alistair Harding for kindly providing us with his streamer geometry reconstruction code. We thank J.P. Canales and J. Conder for their insightful comments that improved this manuscript. The seismic data were processed using "Focus" software of Paradigm Geophysical. This is an Institut de Physique du Globe de Paris contribution (3662).

References

Arnulf, A. F., A. J. Harding, S. C. Singh, G. M. Kent, and W. Crawford (2012), Fine-scale velocity structure of upper oceanic crust from full waveform inversion of downward continued seismic reflection data at the Lucky Strike volcano, Mid-Atlantic Ridge, *Geophys. Res. Lett.*, *39*, L08303, doi:10.1029/2012GL051064.

Arnulf, A. F., A. J. Harding, S. C. Singh, G. M. Kent, and W. Crawford (2013), Nature of upper crust beneath the Lucky Strike volcano using elastic full waveform inversion of streamer data, *Geophys. J. Int.*, doi:10.1093/gji/ggt461.

Arnulf, A. F., A. J. Harding, G. M. Kent, S. C. Singh, and W. C. Crawford (2014), Constraints on the shallow velocity structure of the Lucky Strike volcano, Mid-Atlantic Ridge, from downward continued multichannel streamer data, *J. Geophys. Res. Solid Earth*, *119*, 1119–1144, doi:10.1002/2013JB010500.

Barreyre, T., J. Escartin, R. Garcia, M. Cannat, E. Mittelstaedt, and R. Prados (2012), Structure, temporal evolution, and heat flux estimates from the Lucky Strike deep-sea hydrothermal field derived from seafloor image mosaics, *Geochem. Geophys. Geosyst.*, *13*, Q04007, doi:10.1029/2011GC003990.

Black, J. L., and M. A. Brzostowski (1994), Systematics of time-migration errors, *Geophysics*, *59*, doi:10.1190/1.1443699.

Bohnenstiehl, D., and S. Carbotte (2001), Faulting patterns near 19°30'S on the East Pacific Rise: Fault formation and growth at a superfast spreading center, *Geochem. Geophys. Geosyst.*, *2*, 1056, doi:10.1029/2001GC000156.

Buck, W. R., L. L. Lavier, and A. N. B. Poliakov (2005), Modes of faulting at mid-ocean ridges, *Nature*, *434*, 719–723.

Caine, J. S., J. P. Evans, and C. B. Forster (1996), Fault zone architecture and permeability structure, *Geology*, *24*.

Canales, J. P., J. A. Collins, J. Escartin, and R. S. Detrick (2000), Seismic structure across the rift valley of the Mid-Atlantic Ridge at 23°20'N (MARK area): Implications for crustal accretion processes at slow spreading ridges, *J. Geophys. Res.*, *105*, 28,411–28,425, doi:10.1029/2000JB900301.

Cannat, M. (1993), Emplacement of mantle rocks in the seafloor at mid-ocean ridges, *J. Geophys. Res.*, *98*, 4163–4172, doi:10.1029/92JB02221.

Cannat, M., et al. (1999), Mid-Atlantic Ridge-Azores hotspot interactions: Along-axis migration of a hotspot-derived event of enhanced magmatism 10 to 4 Ma ago, *Earth Planet. Sci. Lett.*, *173*, 257–269.

Chen, J., and G. T. Schuster (1999), Resolution limits of migrated images, *Geophysics*, *64*, doi:10.1190/1.1444612.

Chen, Y. J., and J. Lin (2004), High sensitivity of ocean ridge thermal structure to changes in magma supply: The Galapagos Spreading Center, *Earth Planet. Sci. Lett.*, *221*, 263–273.

Chen, Y., and W. J. Morgan (1990), Rift valley/no rift valley transition at mid-ocean ridges, *J. Geophys. Res.*, *95*, 17,571–17,581, doi:10.1029/JB095iB11p17571.

Christeson, G. L., G. M. Purdy, and G. J. Fryer (1994), Seismic constraints on shallow crustal emplacement processes at the fast spreading East Pacific Rise, *J. Geophys. Res.*, *99*, 17,957–17,973, doi:10.1029/94JB01252.

Christeson, G. L., K. D. McIntosh, and J. A. Karson (2007), Inconsistent correlation of seismic layer 2a and lava layer thickness in oceanic crust, *Nature*, *445*, 418–421.

Combier, V. (2007), Mid-ocean ridge processes: Insights from 3D reflection seismics at the 9°N OSC on the East Pacific Rise, and the Lucky Strike volcano on the Mid-Atlantic Ridge, PhD thesis, Institut de Physique du Globe de Paris, France.

Combier, V., S. C. Singh, M. Cannat, and J. Escartin (2008), Mechanical decoupling and thermal structure at the East Pacific Rise axis 9°N: Constraints from axial magma chamber geometry and seafloor structures, *Earth Planet. Sci. Lett.*, *272*, 19–28, doi:10.1016/j.epsl.2008.03.046.

Crawford, W., S. Singh, T. Seher, V. Combier, D. Dusunur, and M. Cannat (2010), Crustal structure, magma chamber and faulting beneath the Lucky Strike hydrothermal vent field, in *Diversity of Hydrothermal Systems on Slow Spreading Ocean Ridges*, *Geophys. Monogr. Ser.*, vol. 188, pp. 113–132, AGU, Washington D. C.

Crawford, W. C., A. Rai, S. C. Singh, M. Cannat, J. Escartin, H. Wang, R. Daniel, and V. Combier (2013), Hydrothermal seismicity beneath the summit of Lucky Strike volcano, Mid-Atlantic Ridge, *Earth Planet. Sci. Lett.*, *373*, 118–128, doi:10.1016/j.epsl.2013.04.028.

Demets, C., R. G. Gordon, D. F. Argus, and S. Stein (1994), Effect of recent revisions to the geomagnetic reversal timescale on estimates of current plate motions, *Geophys. Res. Lett.*, *21*, 2191–2194, doi:10.1029/94GL02118.

Detrick, R., H. D. Needham, and V. Renard (1995), Gravity anomalies and crustal thickness variations along the Mid-Atlantic Ridge between 33°N and 40°N, *J. Geophys. Res.*, *100*, 3767–3787, doi:10.1029/94JB02649.

Detrick, R. S., J. C. Mutter, P. Buhl, and I. I. Kim (1990), No evidence from multichannel reflection data for a crustal magma chamber in the MARK area on the Mid-Atlantic Ridge, *Nature*, *347*, 61–64.

Dosso, L., H. Bougault, C. Langmuir, C. Bollinger, O. Bonnier, and J. Etoubleau (1999), The age and distribution of mantle heterogeneity along the Mid-Atlantic Ridge (31–41°N), *Earth Planet. Sci. Lett.*, *170*, 269–286.

Dusunur, D. (2008), Thermal structure of mid-ocean ridges (Lucky Strike, Mid-Atlantic Ridge) and magma chambers, PhD thesis, Institut de Physique du Globe de Paris, France.
Dusunur, D., J. Escartin, V. Combier, T. Seher, W. Crawford, M. Cannat, S. C. Singh, L. M. Matias, and J. M. Miranda (2009), Seismological constraints on the thermal structure along the Lucky Strike segment (Mid-Atlantic Ridge) and interaction of tectonic and magmatic processes around the magma chamber, *Mar. Geophys. Res.*, *30*, 105–120, doi:10.1007/s11001-009-9071-3.
Dziak, R., D. Smith, D. R. Bohnenstiehl, C. Fox, D. Desbruyeres, H. Matsumoto, M. Tolstoy, and D. Fornari (2004), Evidence of recent magma dike intrusion at the slow spreading ridge Lucky Strike segment, Mid-Atlantic Ridge, *J. Geophys. Res.*, *109*, B12102, doi:10.1029/2004JB003141.
Escartin, J., P. Cowie, R. Scarle, S. Allerton, N. Mitchell, C. MacLeod, and A. Slootweg (1999), Quantifying tectonic strain and magmatic accretion at a slow spreading ridge segment, Mid-Atlantic Ridge, 29°N, *J. Geophys. Res.*, *104*, 10,421–10,437, doi:10.1029/1998JB900097.
Escartin, J., M. Cannat, G. Pouliquen, A. Rabain, and J. Lin (2001), Crustal thickness of V-shaped ridges south of the Azores: Interaction of the Mid-Atlantic Ridge (36°–39°N) and the Azores hot spot, *J. Geophys. Res.*, *106*, 21,719–21,736, doi:10.1029/2001JB000224.
Escartín, J., S. A. Soule, M. Cannat, D. J. Fornari, D. Düşünür, and R. Garcia (2014), Lucky Strike seamount: Implications for the emplacement and rifting of segment-centered volcanoes at slow spreading mid-ocean ridges, *Geochem. Geophys. Geosyst.*, *15*, 4157–4179, doi:10.1002/2014GC005477.
Forsyth, D. W. (1992), Finite extension and low-angle normal faulting, *Geology*, *20*.
Fouquet, Y., H. Ondréas, J.-L. Charlou, J.-P. Donval, and J. Radford-Knoery (1995), Atlantic lava lakes and hot vents, *Nature*, *377*.
Gale, A., S. Escrig, E. J. Gier, C. H. Langmuir, and S. L. Goldstein (2011), Enriched basalts at segment centers: The Lucky Strike (37°17′N) and Menez Gwen (37°50′N) segments of the Mid-Atlantic Ridge, *Geochem. Geophys. Geosyst.*, *12*, Q06016, doi:10.1029/2010GC003446.
Gente, P., J. Dyment, M. Maia, and J. Goslin (2003), Interaction between the Mid-Atlantic Ridge and the Azores hot spot during the last 85 Myr: Emplacement and rifting of the hot spot-derived plateaus, *Geochem. Geophys. Geosyst.*, *4*(10), 8514, doi:10.1029/2003GC000527.
Goddard, J., and J. Evans (1995), Chemical changes and fluid-rock interaction in faults of crystalline thrust sheets, northwestern Wyoming, USA, *J. Struct. Geol.*, *17*, 533–547.
Harding, A., J. Orcutt, M. Kappus, E. Vera, J. Mutter, P. Buhl, R. Detrick, and T. Brocher (1989), Structure of young oceanic crust at 13°N on the East Pacific Rise from ESPs, *J. Geophys. Res.*, *94*, 12,163–12,196, doi:10.1029/JB094iB09p12163.
Harding, A. J., G. M. Kent, and J. A. Orcutt (1993), A multichannel seismic investigation of upper crustal structure at 9°N on the East Pacific Rise: Implications for crustal accretion, *J. Geophys. Res.*, *98*, 13,925–13,944, doi:10.1029/93JB00886.
Hooft, E., R. Detrick, and G. Kent (1997), Seismic structure and indicators of magma budget along the Southern East Pacific Rise, *J. Geophys. Res.*, *102*(B12), 27,319–27,340, doi:10.1029/97JB02349.
Hooft, E., R. Detrick, D. Toomey, J. Collins, and J. Lin (2000), Crustal and upper mantle structure along three contrasting spreading segments of the Mid-Atlantic Ridge, 33.5°–35°N, *J. Geophys. Res.*, *105*(4), 8205–8226, doi:10.1029/1999JB900442.
Huang, P. Y., and S. C. Solomon (1988), Centroid depths of mid-ocean ridge earthquakes: Dependence on spreading rate, *J. Geophys. Res.*, *93*, 13,445–13,477, doi:10.1029/JB093iB11p13445.
Humphris, S. E., D. J. Fornari, D. S. Scheirer, C. R. German, and L. M. Parson (2002), Geotectonic setting of hydrothermal activity on the summit of Lucky Strike Seamount (37°17′N, Mid-Atlantic Ridge), *Geochem. Geophys. Geosyst.*, *3*(8), 1049, doi:10.1029/2001GC000284.
Ito, G., and J. Lin (1995), Oceanic spreading center hotspot interactions: Constraints from along-isochron bathymetric and gravity anomalies, *Geology*, *23*.
Karson, J. A., G. Thompson, S. E. Humphris, W. B. Bryan, and J. M. Edmond (1987), Along-axis variations in seafloor spreading in the MARK area, *Nature*, *328*, 681–685.
Langmuir, C., et al. (1997), Hydrothermal vents near a mantle hot spot: The Lucky Strike vent field at 37°N on the Mid-Atlantic Ridge, *Earth Planet. Sci. Lett.*, *148*, 69–91.
Lu, L. (1985), Application of local slant stack to trace interpolation, in *SEG Expended Abstracts*, vol. 4, edited by Society of Exploration Geophysicists, pp. 560–562.
McClain, J. S., J. A. Orcutt, and M. Burnett (1985), The East Pacific Rise in cross section: A seismic model, *J. Geophys. Res.*, *90*, 8627–8640, doi:10.1029/JB090iB10p08627.
Mével, C., M. Cannat, P. Gente, E. Marion, J. M. Auzende, and J. A. Karson (1991), Emplacement of deep crustal and mantle rocks on the west median valley wall of the MARK area (MAR, 23°N), *Tectonophysics*, *190*, 31–53.
Miranda, J. M., J. F. Luis, N. Lourenco, and F. M. Santos (2005), Identification of the magnetization low of the Lucky Strike hydrothermal vent using surface magnetic data, *J. Geophys. Res.*, *110*, B04103, doi:10.1029/2004JB003085.
Moreira, M., R. Doucelance, M. D. Kurz, B. Dupré, and C. J. Allègre (1999), Helium and lead isotope geochemistry of the Azores Archipelago, *Earth Planet. Sci. Lett.*, *169*, 189–205.
Morris, E., R. S. Detrick, T. A. Minshull, J. C. Mutter, R. S. White, W. Su, and P. Buhl (1993), Seismic structure of oceanic crust in the western North Atlantic, *J. Geophys. Res.*, *98*, 13,879–13,904, doi:10.1029/93JB00557.
Mutter, J. C., and J. A. Karson (1992), Structural processes at slow-spreading ridges, *Science*, *257*, 627–634.
Newman, P. (1973), Divergence effects in a layered Earth, *Geophysics*, *38*, 481–488.
Ondréas, H., Y. Fouquet, M. Voisset, and J. Radford-Knoery (1997), Detailed study of three contiguous segments of the mid-Atlantic ridge, south of the Azores (37°N to 38°30′N), using acoustic imaging coupled with submersible observations, *Mar. Geophys. Res.*, *19*, 231–255.
Ondréas, H., M. Cannat, Y. Fouquet, A. Normand, P. M. Sarradin, and J. Sarrazin (2009), Recent volcanic events and the distribution of hydrothermal venting at the Lucky Strike hydrothermal field, Mid-Atlantic Ridge, *Geochem. Geophys. Geosyst.*, *10*, Q02006, doi:10.1029/2008GC002171.
Peirce, C., M. Sinha, S. Topping, and C. Gill (2007), Morphology and genesis of slow-spreading ridges: Seabed scattering and seismic imaging within the oceanic crust, *Geophys. J. Int.*, *168*, 59–89.
Phipps Morgan, J., and Y. J. Chen (1993), Dependence of ridge-axis morphology on magma supply and spreading rate, *Nature*, *364*, 706–708.
Pollard, D., and P. Segall (1987), Theoretical displacements and stresses near fractures in rock: With applications to faults, joints, veins, dikes, and solution surfaces, in *Fracture Mechanics of Rock*, Academic Press, London, England.
Reston, T. J., O. Ruoff, J. H. McBride, C. R. Ranero, and R. S. White (1996), Detachment and steep normal faulting in Atlantic oceanic crust west of Africa, *Geology*, *24*.
Rubin, A. M. (1992), Dike-induced faulting and graben subsidence in volcanic rift zones, *J. Geophys. Res.*, *97*, 1839–1858, doi:10.1029/91JB02170.
Rubin, A. M., and D. D. Pollard (1988), Dike-induced faulting in rift zones of Iceland and Afar, *Geology*, *16*.
Salisbury, M. H., and C. E. Keen (1993), Listric faults imaged in oceanic crust, *Geology*, *21*, 413–417.
Scheirer, D., D. Fornari, S. Humphris, and S. Lerner (2000), High-resolution mapping using the DSL-120 sonar system: Quantitative assessment of sidescan and phasebathymetry data from the Lucky Strike segment of the mid-Atlantic Ridge, *Mar. Geophys. Res.*, *21*, 121–142.

Schilling, J.-G. (1985), Upper mantle heterogeneities and dynamics, *Nature*, *314*, 62–67.
Schilling, J.-G. (1991), Fluxes and excess temperatures of mantle plumes inferred from their interaction with migrating mid-ocean ridges, *Nature*, *352*, 397–403.
Seher, T., W. C. Crawford, S. C. Singh, M. Cannat, V. Combier, and D. Dusunur (2010a), Crustal velocity structure of the Lucky Strike segment of the Mid-Atlantic Ridge at 37°N from seismic refraction measurements, *J. Geophys. Res.*, *115*, B03103, doi:10.1029/2009JB006650.
Seher, T., S. C. Singh, W. C. Crawford, and J. Escartin (2010b), Upper crustal velocity structure beneath the central Lucky Strike Segment from seismic refraction measurements, *Geochem. Geophys. Geosyst.*, *11*, Q05001, doi:10.1029/2009GC002894.
Seher, T., W. C. Crawford, S. C. Singh, and M. Cannat (2010c), Seismic layer 2A variations in the Lucky Strike segment at the Mid-Atlantic Ridge from reflection measurements, *J. Geophys. Res.*, *115*, B07107, doi:10.1029/2009JB006783.
Singh, S., W. Crawford, H. Carton, T. Seher, V. Combier, M. Cannat, J. Canales, D. Dusunur, J. Escartin, and M. Miranda (2006), Discovery of axial magma chamber reflections and faults beneath the Lucky Strike volcano and hydrothermal field at the Mid-Atlantic Ridge, *Nature*, *442*, 1029–1032.
Singh, S. C., H. Carton, A. Chauhan, J. Dyment, M. Cannat, N. Hananto, D. Hartoyo, P. Tapponnier, and A. Davaille (2007), Seismic reflection images of deep lithospheric faults and thin crust at the actively deforming Indo-Australian plate boundary in the Indian Ocean, *AGU Fall Meeting Abstracts*.
Sinha, M. C., S. C. Constable, C. Peirce, A. White, G. Heinson, L. M. MacGregor, and D. A. Navin (1998), Magmatic processes at slow spreading ridges: implications of the RAMESSES experiment at 57°45′N on the Mid-Atlantic Ridge, *Geophys. J. Int.*, *135*, 731–745.
Sinton, J. M., and R. S. Detrick (1992), Mid-ocean ridge magma chambers, *J. Geophys. Res.*, *97*, 197–216, doi:10.1029/91JB02508.
Tapponnier, P., and J. Francheteau (1978), Necking of the lithosphere and the mechanics of slowly accreting plate boundaries, *J. Geophys. Res.*, *83*, 3955–3970, doi:10.1029/JB083iB08p03955.
Thatcher, W., and D. P. Hill (1995), A simple model for the fault-generated morphology of slow-spreading mid-oceanic ridges, *J. Geophys. Res.*, *100*, 561–570, doi:10.1029/94JB02593.
Thibaud, R., P. Gente, and M. Maia (1998), A systematic analysis of the Mid-Atlantic Ridge morphology and gravity between 15°N and 40°N: Constraints of the thermal structure, *J. Geophys. Res.*, *103*, 24,223–24,224, doi:10.1029/97JB02934.
Toomey, D., G. Purdy, S. Solomon, and S. Wilcock (1990), The three-dimensional seismic velocity structure of the East Pacific Rise near latitude 9°30 N, *Nature*, *347*, 639–645.
Toomey, D. R., S. C. Solomon, G. M. Purdy, and M. H. Murray (1985), Microearthquakes beneath the median valley of the Mid-Atlantic Ridge near 23°N: Hypocenters and focal mechanisms, *J. Geophys. Res.*, *90*, 5443–5458, doi:10.1029/JB090iB07p05443.
Vogt, P. (1976), Plumes, subaxial pipe flow, and topography along the mid-oceanic ridge, *Earth Planet. Sci. Lett.*, *29*, 309–325.
Von Damm, K. L., A. M. Bray, L. G. Buttermore, and S. E. Oosting (1998), The geochemical controls on vent fluids from the Lucky Strike vent field, Mid-Atlantic Ridge, *Earth Planet. Sci. Lett.*, *160*, 521–536.
Zhang, Y.-S., and T. Tanimoto (1992), Ridges, hotspots and their interaction as observed in seismic velocity maps, *Nature*, *355*, 45–49.